

Controlling the collimation and rotation of hydromagnetic disk winds

Ralph E. Pudritz^{1,2}, Conrad S. Rogers¹, and Rachid Ouyed³

¹ *Department of Physics and Astronomy, McMaster University, Hamilton, ON L8S 4M1, Canada*

² *Origins Institute, McMaster University, Hamilton, ON L8S 4M1, Canada*

³ *Department of Physics and Astronomy, University of Calgary, Calgary, AB T2N 1N4, Canada*

Released 2004 Xxxxx XX

ABSTRACT

We present a comprehensive set of axisymmetric, time-dependent simulations of jets from Keplerian disks whose mass loading as a function of disk radius is systematically changed. For a reasonable model for the density structure and injection speed of the underlying accretion disk, mass loading is determined by the radial structure of the disk’s magnetic field structure. We vary this structure by using four different magnetic field configurations, ranging from the “potential” configuration (Ouyed & Pudritz 1997), to the increasingly more steeply falling Blandford & Payne (1982) and Pelletier & Pudritz (1992) models, and ending with a quite steeply raked configuration that bears similarities to the Shu X-wind model. We find that the radial distribution of the mass load has a profound effect on both the rotational profile of the underlying jet as well as the degree of collimation of its outflow velocity and magnetic field lines. These four models have systematic differences in the power-law rotation profiles of jet material far from the source; $v_{\phi(r)} \propto r^a$ ranging over $-0.46 \geq a \geq -0.76$. We show analytically, and confirm by our simulations, that the collimation of a jet depends on its radial current distribution, which in turn is prescribed by the mass load. Models with steeply descending mass loads have strong toroidal fields, and these collimate to cylinders (this includes the Ouyed-Pudritz and Blandford-Payne outflows). On the other hand, the more gradually descending mass load profiles (the PP92 and monopolar distributions) have weaker toroidal fields, and these result in wide-angle outflows with parabolic collimation. We also present detailed structural information about jets such as their radial profiles of jet density, toroidal magnetic field, and poloidal jet speed, as well as an analysis of the bulk energetics of our different simulations. Our results are in excellent agreement with the predictions of asymptotic collimation for axisymmetric, stationary jets.

Key words: accretion: accretion disks - stars: formation - stars: pre-main-sequence - ISM: jets and outflows - MHD

1 INTRODUCTION

Hydromagnetic disk winds provide what is arguably the most comprehensive quantitative picture for the origin of astrophysical jets in protostellar systems. An extensive body of theoretical work as well as a wide range of numerical simulations, using very different codes, robustly demonstrate that a centrifugally driven wind from an accretion disk can efficiently extract its angular momentum and gravitational potential energy. Disk winds provide a potentially universal mechanism for the origins of jets that are observed in both low and high mass protostars (eg. reviews; Richer et al. (2000); Reipurth & Bally (2001); Zhang (2005); Shepherd (2005)) as well many other systems

such as microquasars (eg. Mirabel & Rodriguez (1998)) and quasars (eg. Begelman, Blandford, & Rees (1984)) because jet properties - such as their terminal velocities and wind mass-loss rates - naturally scale with the depth of the gravitational potential well of the central object and the accretion rate into it (eg. reviews; Spruit (1996); Königl & Pudritz (2000); Pudritz (2003); Pudritz & Banerjee (2005)).

The theory has recently received considerable empirical support by HST observations of the rotation of several jets associated with T-Tauri stars (TTS) (eg. Coffey et al. (2004); Bacciotti et al. (2000, 2002)). High spectral and spatial resolution observations have directly measured the rotation of these jets. The results suggest that the observed

arXiv:astro-ph/0508295v1 12 Aug 2005

jets might have arisen from a region of roughly 1 AU in size in the disk. Moreover, the angular momentum that jets are inferred to carry from this measurement, is a significant fraction that must be carried off to drive the observed accretion rates in the underlying disks. These results seem to agree with the theoretical predictions of disk wind theory (eg., Anderson et al. (2003)).

The observations of jets provoke several important questions about the role of disk winds. How do the underlying accretion disks control jet collimation, even to very large scales? And what determines how rapidly the observed jets spin and the amount of angular momentum that they can extract from the disk? We show in this paper that both of these important properties of jets are aspects of the toroidal dynamics of the jet and are controlled by the same physical process, namely, by the mass loading of the disk wind field lines that occurs near the surface of the disk.

Consider first the issue of jet collimation. The basic mechanism has been understood, at least in principle, for some time. It involves the action of a hoop stress that arises from the generation of a toroidal magnetic field in the rotating, magnetized flow, which pinches the flow towards the outflow axis. The detailed analysis for the collimation of outflows for steady-state jets is extremely difficult since it involves the solution of the highly nonlinear, Grad-Shafranov equation. Progress has been limited to studies of the asymptotic properties of steady state jets (Heyvaerts & Norman 1989) (henceforth HN89), or special self-similar models (eg. Ostriker (1998); Li (1995); Trussoni, Tsinganos & Sauty (1997); Casse & Ferreira (2000)). The general collimation properties of time-dependent jets have, so far, defied general theoretical analysis.

Nature probably produces jets with a range of intrinsic collimations, as suggested by the observations of molecular outflows. Models for observed outflows fall into two general categories: the jet-driven bow shock picture, and a wind-driven shell picture in which the molecular gas is driven by an underlying wide-angle wind component (eg. review Cabrit, Raga, & Gueth (1997)). A survey of molecular outflows by Lee et al. (2000) found that both mechanisms are needed in order to explain the full set of systems observed.

Can the mechanism of jet collimation readily accommodate both possibilities? The simulations of disk winds explore a range of initial magnetic configurations that either originate on the surface of a star and connect with the disk (eg. Hayashi, Shibata, & Matsumoto (1996); Goodson, Winglee, & Böhm (1997); Fendt & Elstner (1999); Keppens00 (2000)), within the disk (eg., von Rekowski & Brandenburg (2004)), or that thread only the disk itself (eg. Ouyed, Pudritz, & Stone (1997); Tomisaka (1998); Kudoh, Matsumoto, & Shibata (2002); Fendt & Čemeljić (2002)). In the former case, twisting of the magnetic field that initially threads the disk beyond the co-rotation radius inflates and then disconnects the field from the star to produce a steeply decreasing, disk-field. In the latter case of purely disk-threaded field, simulations have a variety of initial magnetic geometries: from the split monopole of Romanova et al. (1997), similar to the highly concentrated magnetic field of the Shu et al. (2000) X-wind configuration, to the far more gradual declining or constant magnetic fields featured in the potential solutions investigated by OPS97. The familiar, self-similar disk wind

magnetic geometry of Blandford & Payne (1982; BP82) is intermediate between these two extreme regimes with an initial poloidal magnetic field on the surface of the disk that falls off with disk radius as $B_{BP82}(r_o) \propto r_o^{-5/4}$.

All of these simulations show that outflows are centrifugally driven but that the degree to which they collimate varies. Although the steeply raked, monopolar-like, magnetic field distributions fail to collimate to the outflow axis, they are still candidates for jet models. This is because the densest part of the outflow is directed along those more polar lines giving the appearance of "collimated jets" (even winds from purely dipole stellar field produce this structure; Sakurai (1985); Matt & Balick (2004); Matt & Pudritz (2004)).

We show in this paper that it is the mass loading of a jet - defined as the mass outflow rate per unit magnetic flux - that determines how well jets are collimated. In earlier theory and numerical papers we found that low mass loads for jets lead to rapid, episodic behaviour while more heavily mass-loaded systems tend to achieve stationary outflow configurations (OPS97, Ouyed & Pudritz 1997b (OP97b), Ouyed & Pudritz 1999 (OP99)). This has also been examined in recent work by Anderson et al. (2005).

Regarding the second major issue - angular momentum transport in the jet - we show that this is related to angular momentum extraction by the disk wind torque upon the disk. In steady state, the wind torque depends on the strength of the toroidal magnetic field near the disk surface and this too, we show, depends on how the wind is mass loaded at the disk surface.

We present a series of numerical simulations of jets using a much broader range of initial magnetic configurations than employed in our earlier papers. We vary the mass per unit magnetic flux that threads the disk (the mass loading function) by employing a wide range of initial magnetic field distributions across our disk model. Our initial magnetic configurations range from rather well collimated initial fields (such as the "potential configuration" of OP97a) and the BP82 configuration, to the initially less well collimated configuration of Pelletier-Pudritz (1992; PP92). The final configuration in our simulation suite features an even more steeply declining threading field with disk radius, and is even more open.

One of our major findings is that there are indeed two different kinds of collimation that can be achieved by disk winds with different mass loading profiles: cylindrical collimation and a wide-angle outflow. We provide detailed numerical data that show the radial structure and collimation of a variety of physical variables, including all components of the velocity and magnetic field of the jet, as well as its density profile. We show that this agrees with the predictions that jet collimation is related to the radial structure of the current in these jets, as was first demonstrated analytically by Heyvaerts & Norman (1989, HN89). In fact, the wide-angle flows we find correspond quite well to the case of parabolic collimation predicted in this theory.

We also show that the mass loading of jets affects their radial angular rotation profiles. In particular, we find that the radial distribution of jet rotation is robust and follows radial power-law relations, $v_\phi \propto r^a$, whose index a varies little from model to model: typically in the range $-0.46 \geq a \geq -0.76$ depending on the mass-load profile. These radial

rotation profiles can in principle, be used to discriminate between different disk wind models because the distribution of angular momentum in the wind reflects on how it is mass loaded by the accretion disk at its base.

We begin this paper by first briefly summarizing some recent important observational results on the relation between accretion disks and jets from YSOs (§2) and following this up with a brief review of the basic aspects of hydro-magnetic disk wind theory needed to interpret our numerical results (§3). We then outline our generalized disk wind models which include simulations of BP82 and PP92, and other mass loading profiles, in §4. We analyze our results in §5, and conclude in §6.

2 OBSERVATIONS OF JET STRUCTURE AND DYNAMICS

Of the many important contributions on the issue of jet structure and dynamics, we focus on just a few recent advances that theories and simulations must address. As an example, recent detailed high resolution imaging and spectroscopic studies of jets have revealed their internal dynamical structure in sufficient detail to provide useful constraints on jet theories and numerical simulations. High resolution images of H_α and [OI] emission in the DG Tau jet taken in various velocity ranges from 50 – 450 km s⁻¹ in 125 km s⁻¹ wide velocity bins (Bacciotti et al. 2002) reveal an “onion-like” velocity structure wherein there is a continuous variation in the velocity of the jet, the very highest being the densest and nearest the jet axis, and the lowest farther away. The lower speed flow is farther from the axis and appears to broaden out and become less collimated with increasing radius in the jet. The jet can be traced to within 15 AU (0.1”) of the central source. While earlier papers suggested that jets may have two distinct velocity components (fast and highly collimated, versus slower and wide-angled components Kwan & Tademaru (1988)), the recent data suggest a continuously varying velocity structure.

A second important observed property of jets is that they rotate. For DG Tau as an example, the flow appears to be rotating clockwise when viewed from the flow towards the source (Bacciotti et al. 2003a,b). The rotation speed is 6 - 15 km s⁻¹, depending on the position in the flow within 110 AU from the source. These authors find agreement between these measured rotation speeds with those expected in a centrifugally driven hydromagnetic wind. Using the scalings for disk wind speeds and angular momentum transport rates outlined in §3.1 and §3.2, this outflow is estimated to be carrying up to 60 % of the angular momentum loss from the disk at its footpoint that is needed to drive the observed accretion rate.

Finally, as has been noted many times in the literature, there is a strong correlation between the observed mass accretion rate through protostellar disks and the mass loss rates carried by their jets. Optical jets associated with TTS have typical mass loss rates that are consistently about a tenth of the underlying disk accretion rate. As an example, Hartmann & Calvet (1995) found that for a sample of 31 TTS, jet mass loss rates calculated from the forbidden lines in the range $3 \times 10^{-7} < \dot{M}_j < 10^{-10} M_\odot \text{ yr}^{-1}$ with a median value of $10^{-9} M_\odot \text{ yr}^{-1}$ (eg. review Calvet 2003). These mass

loss rates are a tenth of the underlying disk accretion rate in the system;

$$\dot{M}_j/\dot{M}_a \simeq 0.1. \quad (1)$$

Theory predicts that this is a reflection of the efficient angular momentum extraction from accretion disks by the wind torque.

3 DISK WIND THEORY: JET STRUCTURE AND THE ROLE OF MASS LOADING

The theory of hydromagnetic winds originated with the early work on winds from rotating magnetized stars (eg. Mestel (1968); Weber & Davis (1967)). These papers developed 1-D, axisymmetric models of hydromagnetic flows from rotating stars. The application of this idea to self-similar accretion disks was first carried out in the seminal paper by BP82.

Consider the simplest possible description of magnetized, rotating, conducting gas of density ρ that is threaded by a large-scale field. There are 4 equations of stationary, ideal MHD that describe such a system, namely: the conservation of mass (continuity equation); the equation of motion for gas undergoing a pressure gradient force (from the pressure p), as well as a Lorentz force (from the field \mathbf{B}) - all within in the gravitational field of a central object (whose gravitational potential is ϕ); the induction equation for the evolution of the magnetic field in the moving gas; and finally, the conservation of magnetic flux. These equations were written down by Chandrasekhar, Mestel, and many others:

$$\nabla \cdot (\rho \mathbf{v}) = 0 \quad (2)$$

$$\rho \mathbf{v} \cdot \nabla \mathbf{v} = -\nabla p - \rho \nabla \phi + \frac{1}{4\pi} (\nabla \times \mathbf{B}) \times \mathbf{B} \quad (3)$$

$$\nabla \times (\mathbf{v} \times \mathbf{B}) = 0 \quad (4)$$

$$\nabla \cdot \mathbf{B} = 0 \quad (5)$$

It is convenient to decompose all magnetic fields and velocity fields into poloidal and toroidal field components $\mathbf{B} = \mathbf{B}_p + B_\phi \hat{\mathbf{e}}_\phi$ and $\mathbf{v} = \mathbf{v}_p + v_\phi \hat{\mathbf{e}}_\phi$.

The most basic conservation laws that these equations express are the conservation of mass and magnetic flux (equations 2 and 5). By comparing the form of these two equations, we see that the poloidal field and the poloidal mass flux along the field line must be proportional to one another along a field line. Defining a function k that is a constant along a magnetic field line and which we will call the “mass load” of the wind, then;

$$\rho \mathbf{v}_p = k \mathbf{B}_p \quad (6)$$

This mass load function can be cast in a much more revealing way by noting that the wind mass loss rate passing through an annular section of the flow of area dA through the flow is $d\dot{M}_w = \rho v_p dA$, while the amount of poloidal

magnetic flux through this same annulus is $d\Phi = B_p dA$. Thus, the mass load per unit time, per unit magnetic flux of the wind that is preserved along each streamline along the flow emanating from the rotor (a disk in this case) is

$$k = \frac{\rho v_p}{B_p} = \frac{d\dot{M}_w}{d\Phi} \quad (7)$$

The ultimate source for the mass load is, of course, the accretion disk. While there may be several complicated processes in the disk that prescribe the function k , the stationary theory summarized in equation (7) states that this mass load all comes down to the playoff between the gas density, the injection speed, and the magnetic field strength across the surface of the accretion disk.

The strength of the toroidal magnetic field in the jet plays an important role in jet collimation. We calculate the strength of this field component at any point in a stationary, axisymmetric jet by using the poloidal component of the induction equation which can be written as,

$$B_\phi = \frac{\rho r}{k} (\Omega - \Omega_o). \quad (8)$$

This result shows that the strength of the toroidal field at any point in the flow depends on three things: the relative shear of the flow between the point in question and the foot-point of the field line; the density of the gas (the denser it is the greater the inertia and hence the greater the toroidal field); and finally the mass load. The larger the value of k along a field line, the smaller is the value of the toroidal field, and hence the more diminished role that it plays in collimating the outflow. All else being equal, we expect to have stronger toroidal fields in the portions of an outflow that are fed with smaller mass loads. From this it is clear that the radial distribution of the mass load k in the jet will play a significant role in controlling its collimation.

Now let us turn our attention to the radial rotational profile of a hydromagnetic jet. We derive this from the conservation of angular momentum equation for axisymmetric, stationary flows. This is described by the ϕ component of equation (3), which yields;

$$\rho \mathbf{v}_p \cdot \nabla (r v_\phi) = \frac{B_p}{4\pi} \cdot \nabla (r B_\phi) \quad (9)$$

Let us apply this equation to two different situations - (i) the transport of angular momentum along a field line and (ii) the transport of angular momentum out of a disk, by an outflow (which is analyzed in the following subsection).

By applying equation (6) to equation (9) the angular momentum equation reduces to

$$\mathbf{B}_p \cdot \nabla (r v_\phi - \frac{r B_\phi}{4\pi k}) = 0 \quad (10)$$

This equation says that there is a conserved quantity,

$$l = r v_\phi - \frac{r B_\phi}{4\pi k}, \quad (11)$$

along any given field-line in the flow. This is the total angular momentum per unit mass. The form for l reveals that the total angular momentum is carried by both the rotating gas (first term) as well by the twisted field (second term). Once again, we see that the mass load plays a significant role - here by controlling the relative amount of angular momentum that is carried by the rotation of material in the jet

as compared to that carried by the jet's twisted magnetic field.

The conservation of angular momentum given above, can be rearranged to find the rotational profile of the jet;

$$r v_\phi = \frac{l m^2 - r^2 \Omega_o}{m^2 - 1} \quad (12)$$

where the so-called Alfvén Mach number of the flow is $m = v_p/v_A$ and $v_A = B_p/\sqrt{4\pi\rho}$ is the Alfvén speed of the flow. The Alfvén surface is that point $r = r_A$ at each field line in the wind where $m = 1$. The flow may be regarded as kept in co-rotation with the disk until this point is reached.

The actual value that l takes along any field line is determined by the Alfvén surface where $m = 1$;

$$l(a) = \Omega_o r_A^2 \quad (13)$$

For a field line starting at a point r_o on the rotor (disk in our case), the Alfvén radius is $r_A(r_o)$ and constitutes a lever arm for the flow.

Finally, we note that the conservation of energy in a stationary jet yields a simple relation between the terminal speed of a jet, and the Alfvén radius:

$$v_\infty \simeq 2^{1/2} (r_A/r_o) v_K(r_o) \quad (14)$$

where $v_K(r_o)$ is the Kepler speed at the base of the field line that threads the disk at radius r_o . By combining the conservation laws, one may show that (eg. PP92, Spruit (1996));

$$r_A/r_o = [(B^2/2\pi\rho v_p \Omega_o r_o)^{1/3}] \equiv \mu^{-1/3} \quad (15)$$

The dimensionless parameter μ - which is not a constant along a given field line - has been used as different measure of the mass load of a jet by Anderson et al. (2005).

In general, the conservation laws show that the mass load plays a fundamental role in determining both the collimation as well as the rotational profile of the jet. *Even though direct communication of the jet with the accretion disk is cut off beyond the fast magnetosonic surface of the outflow (which is rather close to the disk) - nevertheless the mass load function is transported from the accretion disk to every point in the outflow. This is how the accretion disk can control the jet's dynamics even far from the source.*

3.1 Jet rotation: angular momentum extraction from the disk

Let us now carry out our second application of the angular momentum equation (9), this time to find the torque that is exerted upon a thin accretion disk by an external field \mathbf{B} . Any vertical flow in the thin disk is negligible so only the v_r contribution matters, and the rotation speed v_ϕ is the Kepler speed if disks are thin. After vertically integrating the equation, noting that the disk accretion rate is $\dot{M}_a = -2\pi\Sigma v_r r_o$. The result is the angular momentum equation for the accretion disk under the action of an external magnetic torque;

$$\dot{M}_a \frac{d(r_o v_o)}{dr_o} = -r_o^2 B_\phi B_z|_{r_o, H} \quad (16)$$

This result shows that angular momentum is extracted out of disks threaded by magnetic fields. By solving for $r B_\phi =$

$k(rv_\phi - l)$ and relations (7) and (11) for k and l the disk angular momentum equation (14) can be cast into its most fundamental form;

$$\dot{M}_a \frac{d(\Omega_o r_o^2)}{dr_o} = \frac{d\dot{M}_w}{dr_o} \Omega_o r_A^2 (1 - (r_o/r_A)^2) \quad (17)$$

As is now well understood, this fundamental equation reveals the crucial link between the mass outflow in the wind, and the mass accretion rate through the disk;

$$\dot{M}_a = (r_A/r_o)^2 \dot{M}_w. \quad (18)$$

The magnetic field forces gas to co-rotate with the underlying disk out to a distance of the order r_A which is why these winds can be so efficient at extracting the angular momentum of the disk. Later in the paper we will show that the typical Alfvén lever arm values in the simulations is $r_A/r_o \simeq 2 - 3$ for a broad range of models. The mean value of the lever arm allows one to calculate the ratio of the wind mass outflow rate compared to the disk accretion rate, $\dot{M}_w/\dot{M}_a \simeq 0.1 - 0.3$.

3.2 Two possible solutions for jet collimation: cylindrically collimated vs "wide-angle" flows

In the standard picture of hydromagnetic winds, collimation of an outflow occurs because of the increasing toroidal magnetic field in the flow as one moves through its various critical points. From equation (8) one deduces that at the Alfvén surface $B_\phi \simeq B_p$, while in the far field (assuming that $r_j \gg r_A$) this ratio is of the order $B_\phi/B_p \simeq r/r_A$. Therefore, collimation can in principle be achieved by the tension force associated with the toroidal field which leads to a radially inwards directed component of the Lorentz force (or "z-pinch"); $F_{Lorentz,z} \simeq J_z B_\phi$.

The radial structure of the outflow is found from the condition of force balance perpendicular to the field lines in the flow, which is known as the Grad-Shafranov equation. This is a very complicated, non-linear equation and no general solutions are known (see review, Heyvaerts (2003)). Because of the mathematical difficulties, analytic studies have been dominated by simplified approaches which focus mainly on finding stationary, self-similar solutions of the flow (eg. BP82, Tsinganos & Trussoni (1990); Li (1995); König (1989); Ostriker (1998); Casse & Ferreira (2000)), or on analyzing the asymptotic limits of the general equations (HN89, PP92).

In HN89 it was shown that two types of solution are possible depending upon the asymptotic behaviour of the total current intensity in the jet;

$$I = 2\pi \int_0^r J_z(r', z') dr' = (c/2)rB_\phi \quad (19)$$

where $\mathbf{J} = (c/4\pi)\nabla \times \mathbf{B}$ is the current density. In the limit that $I \rightarrow 0$ as $r \rightarrow \infty$, the field lines are paraboloids which fill space. On the other hand, if the current is finite in this limit, then the flow is collimated to cylinders. The collimation of a jet therefore depends upon its current distribution - and hence on the radial distribution of its toroidal field - which, as we saw earlier, depends on the mass load. Mass loading therefore determines the asymptotic behaviour of jets!

In order to provide a context for the simulation results to come, it is useful to briefly overview the self-similar model of BP82 in which the disk accretion rate treated as a constant. The only velocity in the self-similar problem is the Kepler speed of the disk. Therefore, one anticipates that the various velocities in the problem scale as $v_A \propto c_s \propto v_r \propto v_\infty \propto v_K$ where one has the Alfvén, sound, radial inflow, terminal wind speed, and Kepler speed all being proportional to one another. Now, the hydrostatic balance condition for thin disk gives $H(r)/r = c_s/v_K$. Therefore, the self-similar scaling $c_s \propto v_K$ implies that $H \propto r$; the disk is wedge-like in its spatial structure. This also implies that the disk temperature follows the virial scaling $T \propto r^{-1}$. The density scaling for the disk follows from the definition of the disk accretion rate, $\dot{M}_a = 2\pi(2H\rho)v_r r$, which given the scaling of the radial inflow velocity $v_r \propto v_K$ and the disk scale height relation implies that $\rho \propto r^{-3/2}$. The wind mass loss rate in the wind follows since the mass loss per unit area along the surface of the disk is $d\dot{M}_w/dA = \rho_o v_{(w,o)} \propto r_o^{-2}$, which implies that $\dot{M}_w(r_o) \propto lnr_o$.

Note that the scaling of the disk Alfvén speed $v_A \propto v_K$, together with the density implies a particular scaling of the disk poloidal field, $B_p \propto r^{-5/4}$. In the BP82 model, the toroidal field on the disk should therefore scale as $B_\phi/B_p = const$, so that $B_\phi \propto r^{-5/4}$. This presents a bit of a dilemma however because the lowest energy toroidal field would be expected to be a force-free condition which has a different scaling $B_\phi \propto r^{-1}$. The Alfvén surface in this model is then $v_\infty/v_K \propto r_A/r_o = const$; ie, a cone. Finally, given the scaling for the disk magnetic field, we can now calculate the mass load of the wind in the BP82 model;

$$k_{o,BP82} \propto r_o^{-3/4}. \quad (20)$$

Jets need not be self-similar structures however. In stationary states, it is perhaps more natural to think of them as having attained minimum energy configurations instead. We have seen above that for the magnetic configuration in which the toroidal field scales as $B_\phi \propto r_o^{-1}$, the current intensity is finite everywhere. The BP82 self-similar solution leads to diverging currents which corresponds to a higher energy state for the magnetic configuration. The disk-wind solutions elucidated by PP92 were designed to characterize non self-similar, minimum energy configurations.

We briefly remind the reader of the motivation for the PP92 solution by first writing down the general Grad-Shafranov (GS) equation for stationary, axisymmetric flow, for the surfaces of magnetic flux $a(r, z)$ in the flow. Magnetic field lines are restricted to surfaces of constant magnetic flux, $a(r, z) = const$, where the the poloidal magnetic field follows from the relation $\mathbf{B}_p = (1/r)\nabla(a) \times \hat{\phi}$. The GS equation can be written in a suggestive form (see PP92):

$$\frac{r^4}{m^2} (\nabla \cdot \frac{m^2 - 1}{r^2} \nabla a) = \lambda(a) \bar{\eta}(a) a \quad (21)$$

where the function $\bar{\eta}(a) \simeq const$ and the function

$$\lambda(a) \equiv \frac{\Omega_o^2 r_A^2}{v_A^2} c_A = \frac{4\pi\rho_A(a)\Omega_o^2 r_A^6}{a^2} \left(\frac{dlnr_A}{dlna} \right)^2 \quad (22)$$

is a constant on a surface of constant magnetic flux and depends upon the density at the Alfvén point, ρ_A . Solving this last relation for the Alfvén radius, we see that $r_A \propto \lambda^{1/6}$ which is such a weak dependence that solutions with $\lambda = const$ were sought (PP92).

The accretion disk imposes an important set of boundary conditions on the GS equation that includes the value of the magnetic flux function across its surface; $a(r, z) = a_o(r_o, z_o)$. Without loss of generality, one may assume that the flux takes on a power-law form on the disk;

$$a_o \propto r_o^{\mu+1}. \quad (23)$$

so that the poloidal field threading the disk, which is derived from this flux, becomes

$$B_z(r_o, 0) = br_o^{\mu-1}. \quad (24)$$

The general form of the GS equation given above can be exploited by using the Ansatz that $\lambda = const$, as shown by PP92. In this regime, we find many of the interesting solutions including the self-similar case of BP82. The GS equations show that the Alfvén surface takes the form:

$$r_A/r_o \propto a^{[4(\mu+1)-3]/[2(\mu+1)]} \propto r_o^{2\mu+(1/2)} \quad (25)$$

while the current takes the form

$$I(r, z) \propto a^{[1-2(\mu+1)]/[2(\mu+1)]} \propto r_o^{-\mu-(1/2)}. \quad (26)$$

This result for the radial current distribution contains the key insight about the collimation of jets from accretion disks. We note that there are two distinct categories of mass loads that by the HN89 theorem, will have different collimation properties: *For magnetic field distributions with $-1/2 > \mu$; the radial current profile diverges,*

$$\lim_{r \rightarrow \infty} I(r) \rightarrow \infty; \quad (27)$$

so that wide-angle flows are to be expected. On the other hand, *distributions with $-1/2 < \mu$ have currents that vanish at infinite radius,*

$$\lim_{r \rightarrow \infty} I(r) \rightarrow 0 \quad (28)$$

so that the flow should collimate to cylinders.

The particular state investigated by PP92 is the unique case in which the current is finite, but does not diverge; $\mu = -1/2$, whose radial current profile is

$$I_{PP92} = const, \quad (29)$$

and poloidal field profile in the disk is $B_p \propto r_o^{-3/2}$. The Alfvén surface for the PP92 model scales as $(r_A/r_o)_{PP92} \propto r_o^{-1/2}$, while the terminal speed in this solution has the behaviour $v_{\infty} \propto r_o^{-1}$. Finally, the mass loss rate in the wind for the PP92 solution is $\dot{M}_w \propto [(r_o/r_i) - 1]$, where r_i is the inner edge of the disk. The mass loading of this model wind scales as

$$k_{o,PP92} \propto r_o^{-1/2}. \quad (30)$$

How does an accretion disk establish the radial profile of the outflow mass load function, $k(r_o)$? The density at the disk surface is prescribed by the hydrostatic balance condition with the base of the disk corona above it (the initial condition we have used in our own simulations, see §4). In reality, we expect that the jet originates from some region in the disk corona so that the principle of hydrostatic balance between the disk and the base of the corona should remain reasonably secure. The second factor in the mass load is the injection speed of material into the base of the outflow, v_{inj} . This speed must be subsonic in magnitude. We consider that the most natural scaling of this injection speed

is with the local Keplerian velocity at each radius of the disk; typically $v_{inj} = 10^{-3}v_K$ at any point on the disk. These two physically reasonable conditions imply that the main factor in determining the mass loading of the disk wind is actually the radial distribution of the threading magnetic field across the disk. Assuming a power-law scaling of this poloidal field component given above, we find that the mass load function at the disk surface follows a power law relation;

$$k(r_o) = \rho_o v_{p,o} / B_{p,o} \propto r_o^{-1-\mu} \quad (31)$$

How do the mass loads of the different wind models compare? For the BP82 and PP92 mass-load functions as an example: the PP92 mass loading function is a less steeply raked function of disk radius than the BP82 self-similar case (wherein $k_{BP82} \propto r_o^{-3/4}$). The associated current profile for the BP82 solution (which can also be found from equations (19) and (20) above (with $\lambda = const$) and pertains to the case $\mu = -1/4$. The current profile in the BP82 theory is therefore

$$I_{BP82} \propto r_o^{-1/4}. \quad (32)$$

The essential point is that whereas the BP82 current $I(r)_{BP82} \rightarrow 0$ as $r \rightarrow \infty$, the Pelletier-Pudritz has a finite current in this limit $I(r)_{PP92} \neq 0$. This implies that yet steeper mass load profiles and more generally, the monopole-like magnetic configuration of models like Romanova et al. (1997), and the X-wind of Shu et al. (2000), should diverge in this limit. The mass load of these latter models produces a toroidal magnetic field that is strongly concentrated towards the outflow axis, with little left in the wide-reaches of the outflow to effectively collimate the outflow to the axis.

Thus, we have shown that by using the HN89 limit together with the theory of mass loading shown above, that the PP92 case should provide a dividing line between jets that ultimately collimate to cylinders, and jets whose magnetic and streamlines are parabolic and therefore "wide-angled". This result implies that disk winds can in principle provide a wide-angle pressure that can drive molecular outflows, and that this is essentially determined by how the accretion disk mass-loads the jet.

4 NUMERICAL SIMULATIONS - INITIAL CONDITIONS

Our numerical approach in this paper is a generalization of the method used in our earlier papers (OPS97, OP97a,b; OP99). Conditions on the underlying accretion disk remains constant in time and provide a set of fixed boundary conditions for the outflow simulation. Several groups have exploited this approach (eg. Ustyugova et al. (1998); Romanova et al. (1997); Meier et al. (1997); Krasnopolsky, Li, & Blandford (1999); Fendt & Čemeljić (2002)). The published simulations differ in their assumed initial conditions, such as the magnetic field distribution on the disk, the plasma β ($\equiv P_{gas}/P_{mag}$) above the disk surfaces, the state of the initial disk corona, and the handling of the gravity of the central star.

We used the ZEUS 2-D code which is arguably the best documented and utilized MHD code in the literature

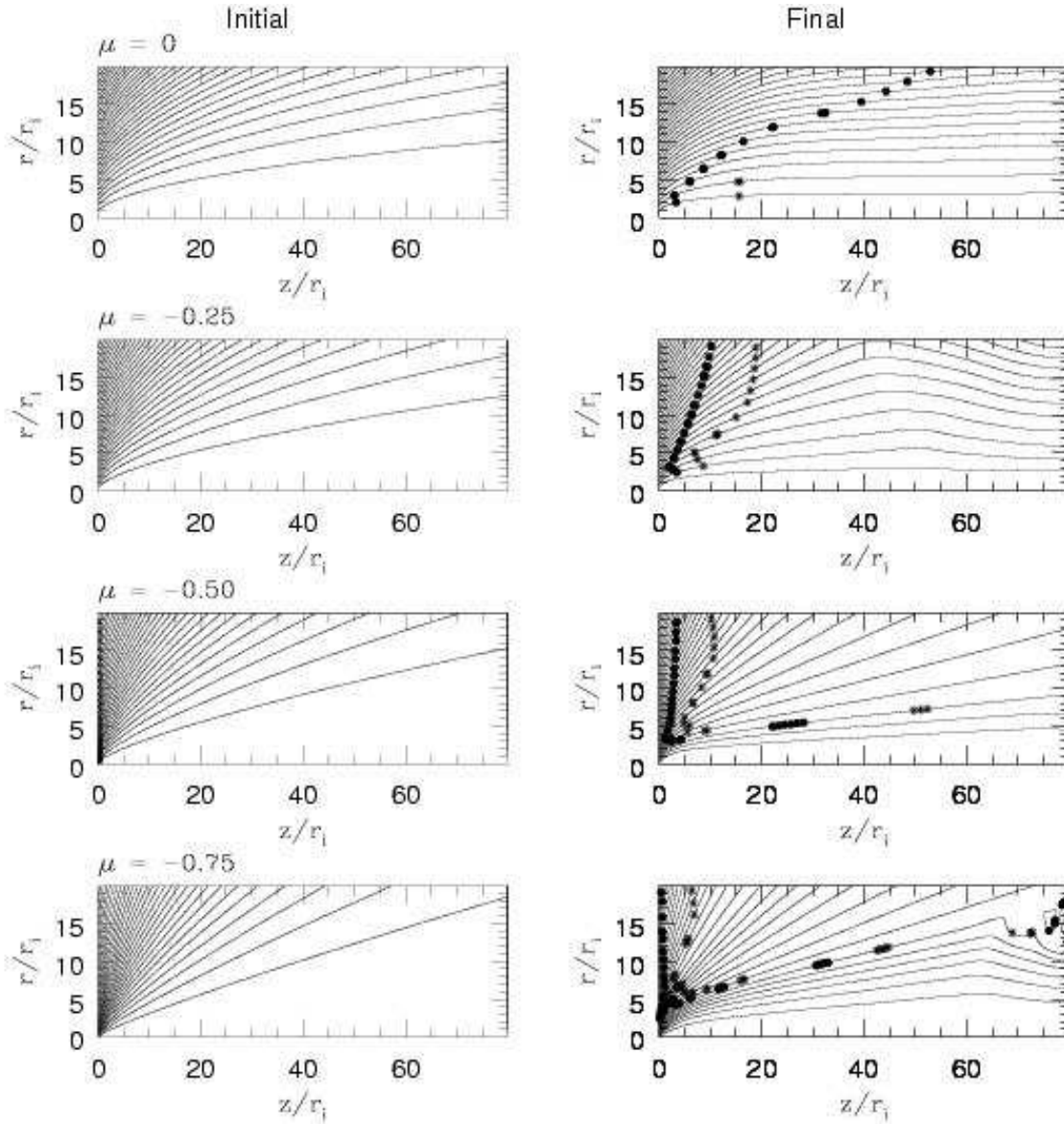
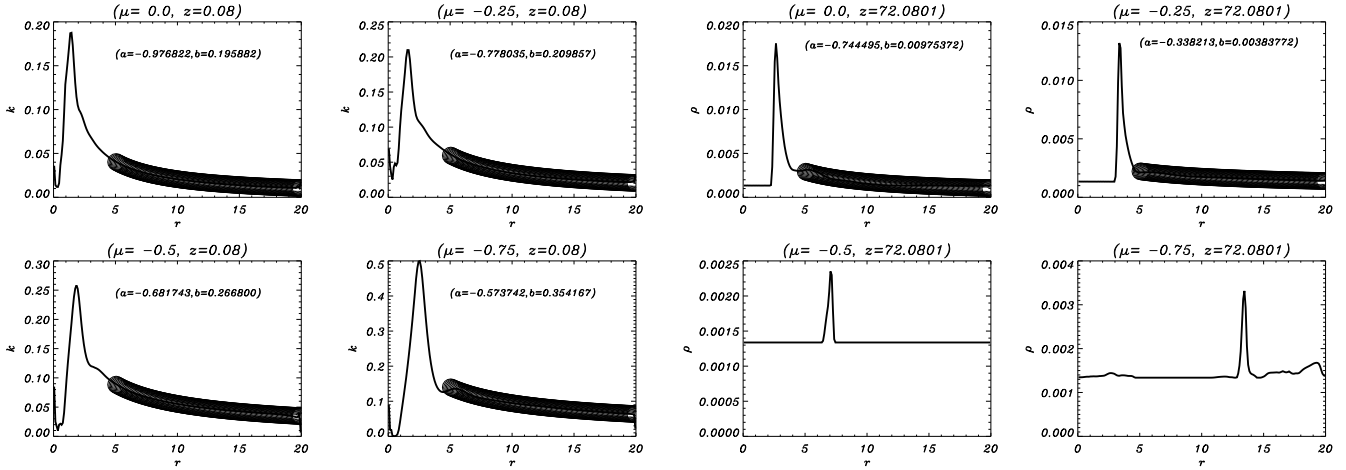


Figure 1. Left panels: initial magnetic field configurations for winds with initial potential ($\mu = 0$), Blandford & Payne ($\mu = -0.25$), Pelletier & Pudritz ($\mu = -0.5$), and 7Q ($\mu = -0.75$) configurations shown. Right panels: final magnetic field configurations (at $t = 400$) for each case, with Alfvén points (filled circles) and FM points (stars) marked. Note the more open magnetic - and stream line structures as the initial magnetic configuration (value of μ) changes.

(Stone & Norman (1992, 1994)). It is an explicit, finite difference code that runs on a staggered grid. The evolution of the magnetic field is followed by the method of constrained transport. In this approach, if $\nabla \cdot \mathbf{B} = 0$ holds for the initial magnetic configuration, then it remains so for all later times to machine accuracy. The obvious way of securing this condition is to use an initial vector potential $\mathbf{A}(\mathbf{r}, \mathbf{z}, \mathbf{t} = 0)$ that describes the desired initial magnetic field at every point in the computational domain.

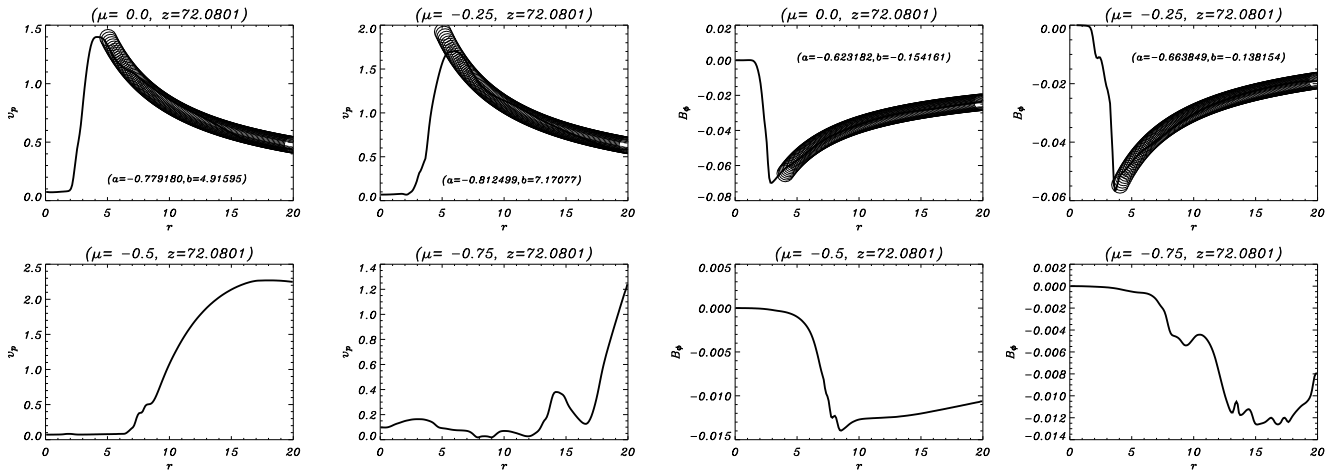
The accretion disk in all of our work so far is chosen to be initially surrounded by a polytropic corona ($\gamma = 5/3$) that is in hydrostatic balance with the central object. We do this because it is the equation of state used in BP82 which provides an invaluable analytic and numerical solution

to which we can compare our simulations. The accretion disk at the base of the corona is given a density profile that it maintains at all times in the simulation, since the disk boundary conditions are applied to the "ghost zones" and are not part of the computational domain. It is chosen so that the disk surface is in pressure balance with the corona above it (ie. $\rho \propto r_o^{-3/2}$ for a $\gamma = 5/3$ model - as in BP82). This hydrostatic state has a simple analytic solution which was used as the initial state for all of our simulations.



(a) Radial dependence of the mass loading parameter, k at the disk surface. The first two cases fit the predicted behaviour; $k \propto r^{-1-\mu}$. (A power law form $\psi = br^a$ is the fit used for any physical quantity ψ).

(b) Radial dependence of density for each configuration at high z . The peak density (which defines the jet) in the first two cases is about an order of magnitude greater than latter two, and is collimated closer to the disk axis.



(c) Radial dependence of the poloidal velocity at high z . The collimated flows show higher velocities closer to the disk axis, whereas the non-collimated solutions have almost the opposite behaviour, indicative of a wide-angle wind.

(d) Radial dependence of the toroidal magnetic field for each configuration at high z . The maximum value is close to the disk axis in the first two cases, as expected for a collimated wind. The last two cases exhibit a much weaker field strength, explaining why these flows show no collimation.

Figure 2. Radial profiles of physical quantities at $t = 400$. The cuts shown in the upper left panel, (a), were taken at $z \simeq 0.0$ close to the disk surface while the cuts in panels (b), (c) and (d) were taken further out at $z \simeq 72.0$.

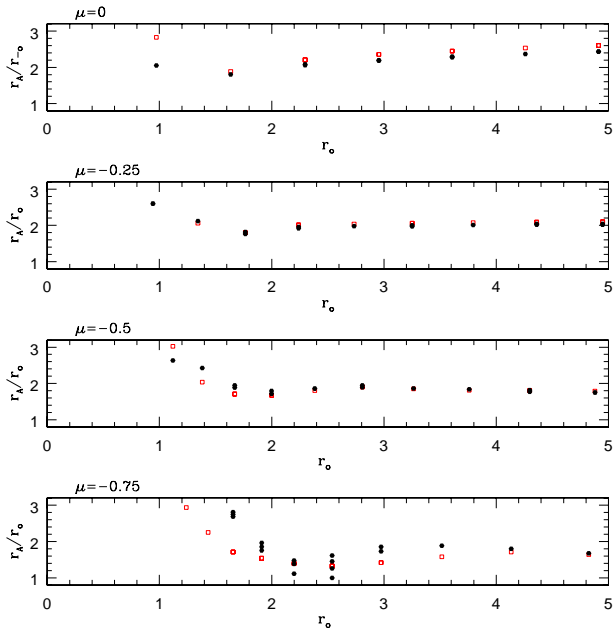


Figure 3. The Alfvén lever arm for the four configurations, at $t = 400$, as compared to the prediction from steady-state theory (squares).

The initial magnetic configurations in our studies are chosen so that no Lorentz force is exerted on the initial (non-rotating) hydrostatic corona described above; more specifically, we used initial current-free configurations $\mathbf{J} = 0$ in the computational domain. The initial vector potential is subject to the boundary condition on the disk that the poloidal field on the disk surface $(r_o, 0)$ has a power-law form and field structure given by equations (23) and (24) respectively.

An analytic solution for the field throughout the computational volume can be found for the choice $\mu = 0$ on the disk. This is the so-called "potential" configuration that we used in several of our papers. We can accommodate more general initial magnetic configurations however, by using a Hankel transform technique to solve for the initial vector potential that is subject to these constraints (see Appendices A and B for details). We chose our particular Hankel transform method as the one that best maintained the initial equilibrium state for arbitrary amounts of machine time (see Appendix B). We always use an unsoftened gravitational potential from the central object. The initial corona is ultimately swept away by the disk wind in all of these simulations so that the mass source for our jets becomes dominated by the material injected from the fixed disk below.

We simulated a representative set of models by choosing an initial BP82 model ($\mu = -1/4$), PP92 ($\mu = -1/2$), and a yet more steeply declining magnetic field such as $\mu = -3/4$ (referred to as the 7Q configuration). These initial configurations are plotted out in the left panels of fig. 1. From the current profile given in equation (24), we would predict that if these flows settle into a stationary state, then the models with $\mu = 0; -1/4$ should be cylindrically collimated while the remaining two models; $\mu = -1/2; -3/4$ should be "wide-angle" or parabolically collimated flows. This was our

rationale in choosing these special, illustrative models. The mass loading functions corresponding to these four magnetic field distributions are progressively less steeply raked; going from:

$$k(r_o) \propto r_o^{-1}, \quad r_o^{-3/4}, \quad r_o^{-1/2}, \quad r_o^{-1/4} \quad (33)$$

respectively.

Our simulations of thin disks require that we specify five physical quantities at all points of the disk surface at all times. There are the disk density $\rho(r_o)$; components of the vertical and toroidal magnetic field, $B_z(r_o)$ and $B_\phi(r_o)$; and velocity components in the disk, $v_z(r_o)$ and $v_\phi(r_o)$. The remaining field component $B_r(r_o)$ is determined by the solenoidal condition while the radial inflow speed through the disk $v_r(r_o) \simeq 0$ for the purposes of the simulations since it is far smaller than the sound speed in a real disk. The model is described by five parameters, whose values describe conditions at the inner edge of the disk at radius $r_o = r_i$. Three of these parameters describe the initial corona: β_i which is typically $1/3$ (and which therefore falls with radius); the density jump across the corona/disk boundary η_i which is typically 100; and ratio of the Keplerian to thermal energy density δ_i , set to be 300 initially. Two additional parameters describe the disk physics. The parameter, ν_i , which scales the toroidal field in the disk $B_\phi = \nu_i/r_o$, was found to be unimportant. We emphasize that this last initial condition plays no role in the subsequent evolution of the simulation - even if the initial toroidal field on the disk surface vanishes, the wind itself quickly generates the self-consistent field. We have never observed that this parameter is important.

We ran high resolution simulations in which (500×200) spatial zones were used to resolve a physical region of $(80r_i \times 20r_i)$ in the z and r directions, respectively. Our simulations ran up to $400t_i$ (where t_i is the Kepler time for an orbit at the inner edge of the disk, r_i). The standard parameter settings were

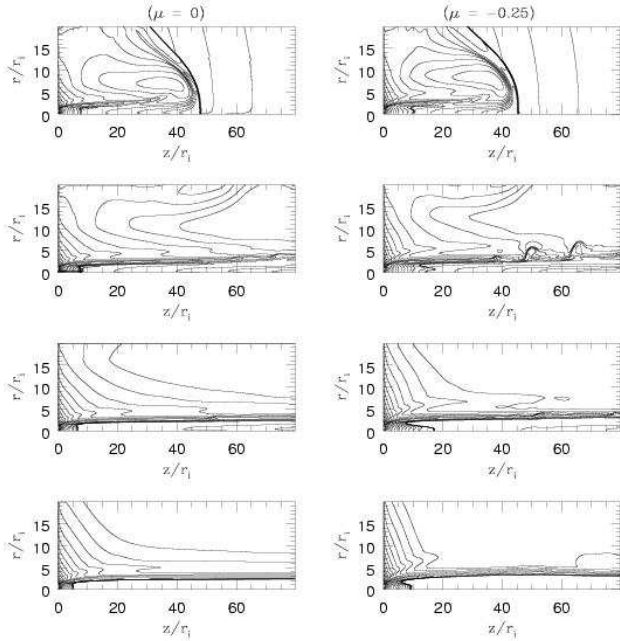
$$(\eta_i, \nu_i, v_{inj}, \delta_i, \beta_i) = (100.0, 1.0, 0.001, 300.0, 1/3) \quad (34)$$

We focused our simulations on the four initial magnetic field configurations discussed above - which between them give a very broad range of mass load profiles and behaviours for the jets. We found that we could only run the BP82 configuration to $t = 400$, and barely that, as the simulation ground down terribly. Once the density in the corona had been cleared out, the Alfvén velocity went very high, making the timestep prohibitively small. This was also a problem with the PP92 case. Since the 7Q case never really blew out a lot of material, we managed to run it out to $t = 500$.

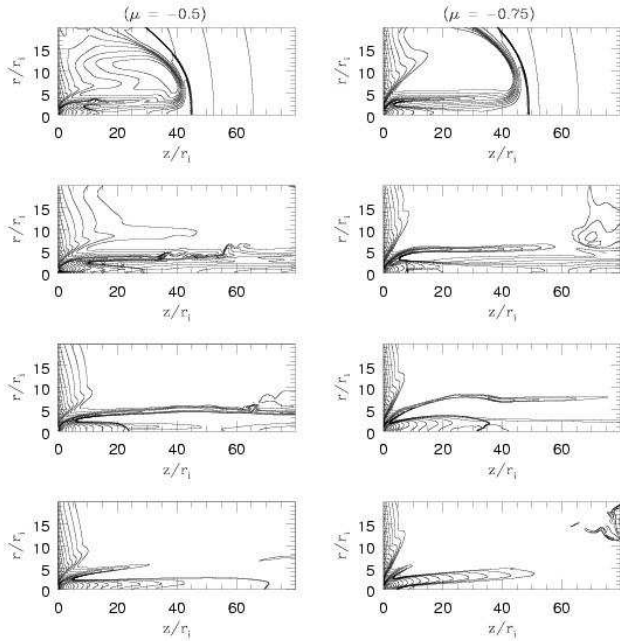
5 RESULTS

5.1 Jet collimation - magnetic field lines, density, and velocity behaviour

Figure 1 plots the magnetic field lines of both the initial states of each model (left panels) as well as the final states of simulations. In addition to the potential case ($\mu = 0.0$), simulations of the Blandford-Payne ($\mu = -0.25$), Pelletier-Pudritz ($\mu = -0.5$), as well as an even more steeply raked ($\mu = -0.75$) initial magnetic configuration are shown. It is evident that the field lines in these right hand panels are



(a) Density structure of jets from the potential ($\mu = 0$, left panels), and Blandford-Payne ($\mu = -0.25$, right panels) solutions. Note the densest material moves along the jet axis.



(b) The corona has been cleared out by the uncollimated disk wind. The 'jets' from the Pelletier-Pudritz ($\mu = -0.5$, left panels), and steeper ($\mu = -0.75$, right panels) solutions should be compared to the velocity profiles in Fig. 3

Figure 4. Contours mark surfaces of constant density in the jet at four different times ($t = 60, 120, 200, 400$).

progressively less well collimated towards the axis, suggestive of a wide angle flow at larger radii. A careful examination shows that while the potential and BP82 cases achieve cylindrical collimation within our computational grid, the PP92 and 7Q cases remain more "open". While collimation may still occur on spatial scales much larger than our computational volume, this is difficult to investigate because of the very small time step required in regions of large Alfvén speeds. We see a difference in collimation behaviour that agrees with the predictions of steady-state jet theory that we outlined in §3.2. It appears that the PP92 case is the transition between solutions that collimate to cylinders, and those that have parabolic structure in the asymptotic limit.

Figure 1 also shows the positions of the Alfvén surfaces for each configuration marked on the field lines. The BP82 final state shows that the Alfvén surface is indeed nearly a cone as expected while the PP92 simulation qualitatively agrees with the expected scaling $r_A \propto r_o^{1/2}$ (see §3.2). The details of the outflow for the "potential" configuration are found in OPS97 and OP97a.

The mass load function for these models is shown in Figure 2(a) wherein the values of the function $k(r, z)$ are numerically tabulated along a radial spatial cut through the flow that is a few pixels above the disk inside the computational zone. In stationary state, the mass loads should settle down to power-law radial distributions that match the input at the surface of the disk, predicted in equation (31). The figure shows power-law fits for physical quantities ψ (in this case, $\psi = k$) of the form

$$\psi = br^a \quad (35)$$

which give for the 4 different magnetic configurations (always starting with the potential configuration $\mu = 0$), $a = -0.98, -0.78, -0.68, -0.57$, which compares favourably with the predictions except for the last case, the 7Q model. The simulations of the potential flow and the BP82 outflows have settled into stationary states so that the mass loads in the jet closely give the input value at the disk surface (-1.0 and -0.75 respectively). The PP92 simulation has not settled down completely by the end of our run, but well enough that there is a good correspondence with the predicted load profile of -0.5 compared to our numerical value -0.68. The greatest discrepancy is found for the 7Q run, but as noted, this has not achieved a completely stationary state even by the end of $t = 400$.

A quantitative analysis of the radial density behaviour of these 4 outflows is given in Figure 2(b). The potential and BP82 configurations have greater peak densities than the PP92 and 7Q models. Another difference appears to be that whereas the former two have a declining power-law density behaviour with

$$a = -0.74 \quad (\mu = 0); a = -0.34 \quad (\mu = -1/4) \quad (36)$$

- the potential and BP82 cases respectively - the radial behaviour is quite different in the PP92 and 7Q cases which appear to be nearly independent of radius. In every case, there is a central "spike" in the gas density which is the material at the smallest radius that moves more parallel to the outflow axis. The radial position of this "spike" moves outward in radius as one can see from the figures.

The corresponding radial behaviour of the poloidal ve-

locity is analyzed in Figure 2(c) by means of a spatial cut through the flow taken most of the way down the jet at $z = 72.08$. The peak speed in each of the first 3 models increases. There is also a distinct fall-off in jet outflow speed with disk radius, which for the potential and BP82 cases behave as

$$a = -0.78, \quad a = -0.81; \quad (37)$$

which are virtually identical. It is evident from this figure that the PP92 and 7Q cases have a larger "hole" in the middle of their jets, and that their poloidal speeds fall off less steeply with jet radius.

The radial profile of the toroidal magnetic field for the models is shown in Figure 2(d). In all of our simulations, the toroidal field must vanish on the rotation axis. It reaches a peak value at the inner edge of the outflow and then declines. This means that the toroidal magnetic field pressure exerts an inward pressure force from this peak, and an outwards pressure gradient force at larger radii than the peak radius (see OP97a). While the potential and BP82 cases have similar radial power law behaviour for the toroidal field; $B_\phi(r) \propto r^{-0.64}$ on average at the larger radii, the PP92 and 7Q cases have much weaker toroidal fields everywhere.

We compare the predicted structure of the Alfvén surface and that from theory in Figure 3 where we plot the Alfvén lever arm versus the footprint radius of a given field line. The analysis of equation (25) predicts that as one goes from $\mu = 0 \rightarrow \mu = -3/4$, then

$$r_A/r_o \propto r_o^{1/2}, \quad const., \quad r_o^{-1/2}, \quad r_o^{-1} \quad (38)$$

respectively. The first three solutions compare well to the theory. The steepest case has its Alfvén surface too close to the disk surface to be well-resolved, which may explain the discrepancy. We see that the Alfvén lever arm usually lies within the domain of 2-3 in value for the innermost field lines of the flow.

The evolution of the density structure of these jets is shown in the snapshots presented in Figures 4(a)–4(b) for 4 different times ($t = 60, 120, 200, 400$). In each simulation, we see the jet driving a bow shock through the quiescent gas in the first frame. In the second frame the shock has just moved out of the grid. In all four of these simulations, one clearly sees that the densest gas in the jet is always well collimated and moving nearly parallel to the axis. This is a general consequence of any reasonable mass loading for a jet. Thus, whether or not the outflow has a wide-angle aspect to it or not, the bulk of the material that we see in all of our simulations moves along in a fairly concentrated and collimated manner. Thus, all of our simulations when observed in appropriate forbidden line emission, would appear "jet-like" - as first noted by Shu et al. (2000) for their X-wind simulations.

The poloidal velocity vectors associated with these outflows is shown in Figures 5(a)–5(d). The four frames shown in each of these panels correspond to the 4 times shown in Figs. 4(a)–4(b). A well-collimated jet is visible in the velocity figures for the first two cases - potential and BP82 outflows. In the fourth case (7Q) we see that whereas the jet density is highly collimated (Fig. 4b, right panel) along the axis - a wide-angle velocity profile is obvious. Thus, the bulk of the jet material follows the few field lines that have collimated parallel to the disk axis, but is clearly sub-Alfvénic. The

bulk of the kinetic energy of the flow is in the wide-angle wind. Thus, the PP92 and 7Q cases represent two models in which a wide-angle component could carry momentum sufficient to produce a wide-angle molecular outflow. The final stage ($t = 400$) of the PP92 solution resembles the 7Q case more closely than either of the well-collimated solutions.

Taken together, Figures 2–5 show the existence of two regimes of disk-driven winds; one that results in a highly collimated jet, and the other that produces a wide-angle wind. The PP92 configuration seems to be a transitional model lying between these two distinct regimes. In all situations, the bulk of the flow's mass density is fairly well collimated along the flow axis. The cylindrical or parabolic collimations ($\mu = 0, -1/4$ and $\mu = -1/2, -3/4$ cases respectively) primarily affect the velocity field and a small amount of the gas in the outflow.

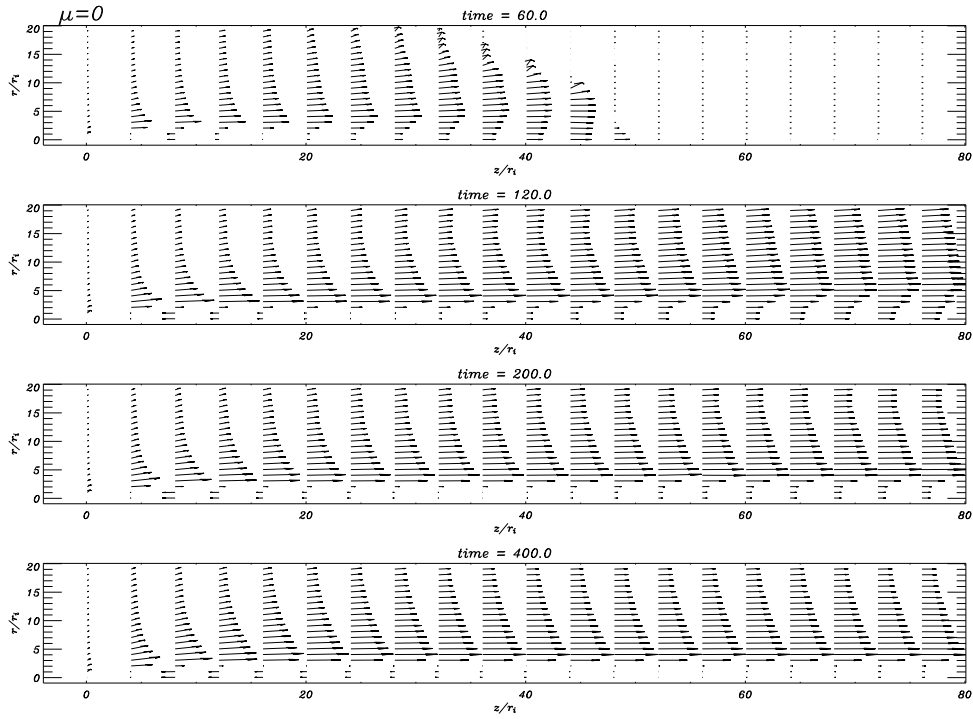
5.2 Jet dynamics - moving along a field line

In Figs. 6(a)–6(d), we trace the behaviour of physical quantities along the fifth innermost fieldline which is chosen since it remains on the computational mesh and is concentrated more towards the central axis of the flow. Comparing the upper-left panel for each configuration, we see that the potential case reaches an Alfvén Mach number of about 1.5, but never reaches its fast magnetosonic speed. The BP82 case accelerates much more quickly, and has reached its fast magnetosonic point at $z = 1.5$, reaching a peak Alfvén Mach number of 7 before the poloidal velocity levels off.

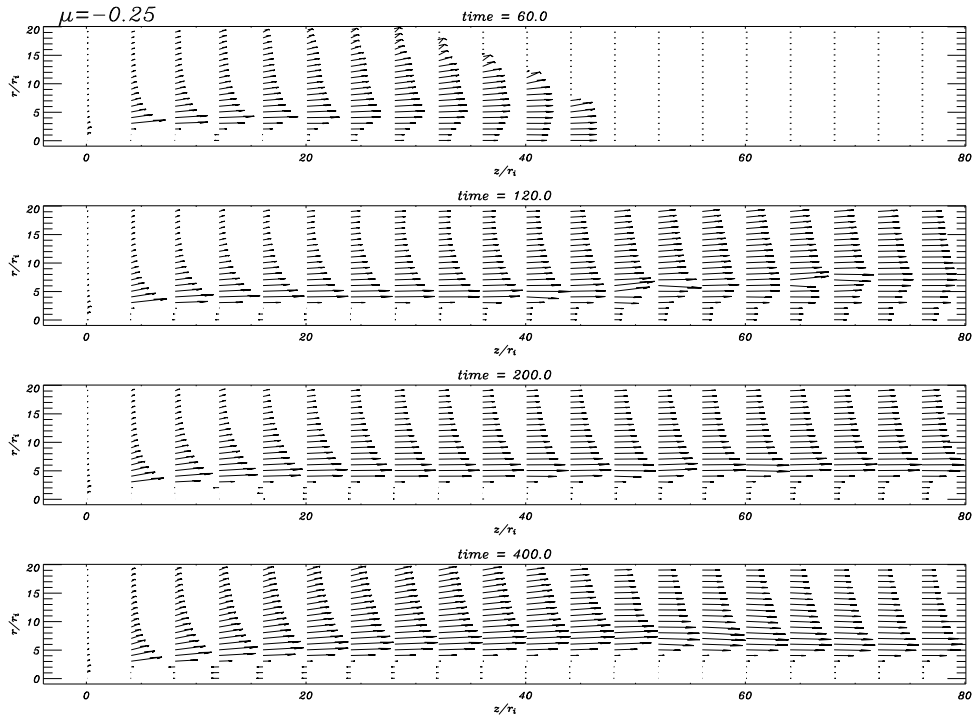
The PP92 configuration reaches a very high Alfvén Mach number of nearly 50 before it undergoes an abrupt downturn in value. The 7Q case does not really seem to settle into as stationary a configuration, but the results do seem to suggest that it is in a different regime of Alfvén Mach number.

The rather abrupt decrease in the outflow Mach numbers seen in this figure arises from the presence of shocks and knots along the innermost field lines. This is evident from an examination of the Alfvén and FM points along inner field lines shown in Figure 1. While the potential flow seems to have reached a very stable, stationary state by the end of the simulation, the BP82 and PP92 simulations require increasingly longer times to settle into stationary flows while the 7Q case did not settle into a stationary state in the far field region at $z/r_i \geq 60$. Another indication that shocks are responsible for these abrupt changes is that the toroidal to poloidal magnetic field, as well as the value of the toroidal flow velocity, also undergo similar sharp changes in value.

The outflow velocity along the field line, in units of the Kepler speed at the foot of the field line, increases for these first three models. Thus the highest speed flow in the centre-most region of a jet arises in the PP92 model, more even than the BP82 solution. As for the rotation speed of material in the outflow, it always falls to a fraction of its initial value, as theory predicts (because of the expansion of the flow, as well as the transport of angular momentum that is carried by the twisted field). We defer our analysis to the radial rotational profile of material in the jet to §5.4 below.

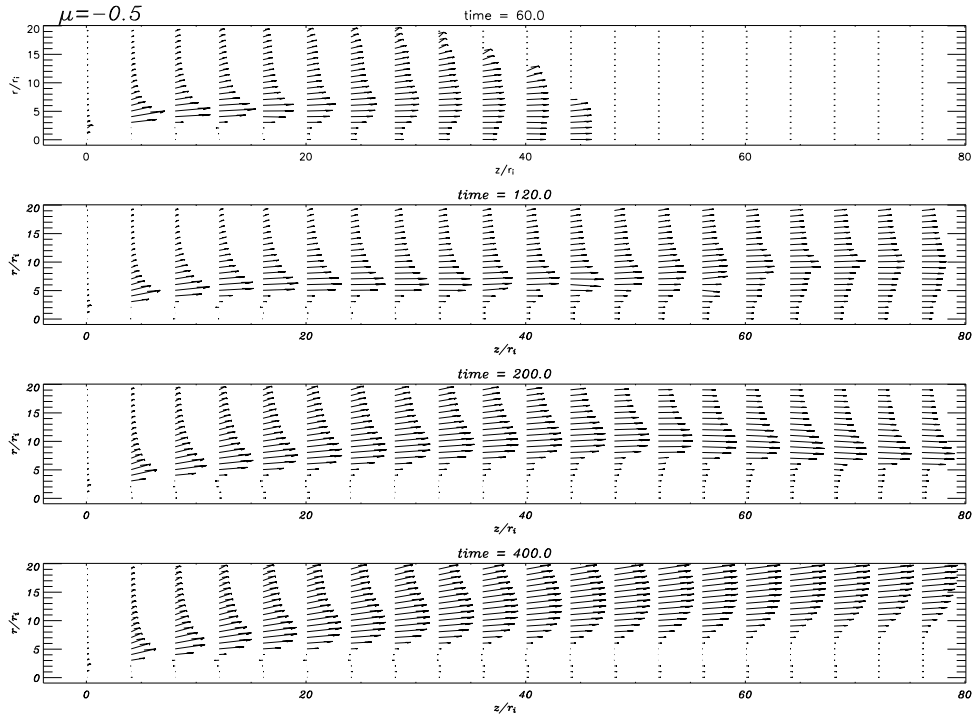


(a) Potential case: Note that the highest velocities are nearest the outflow axis, and that the flow is very well-collimated

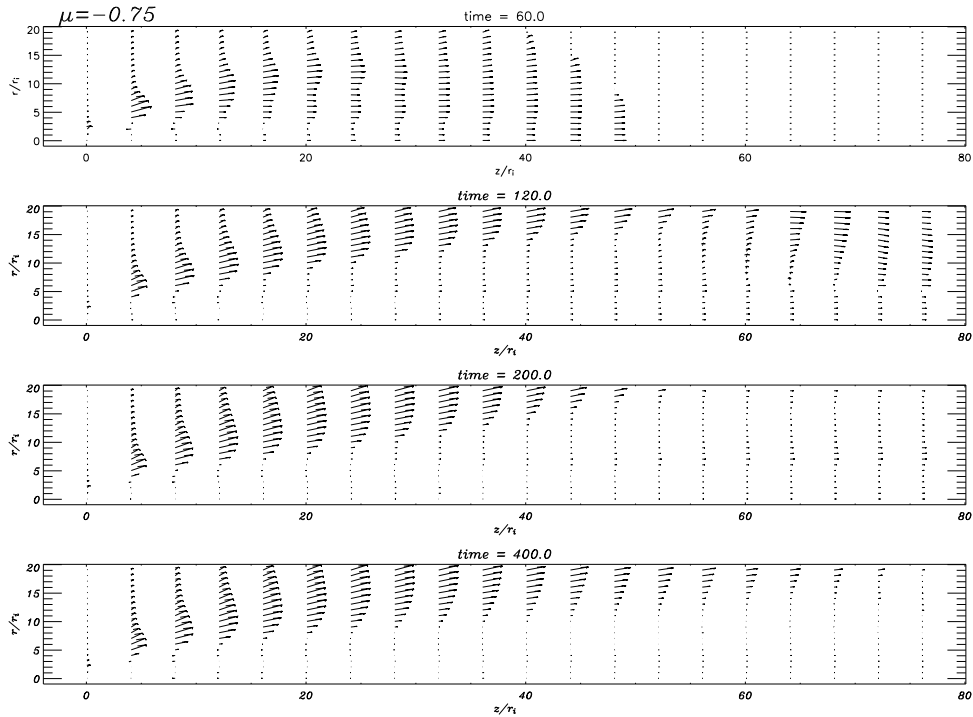


(b) BP82 case: Note that the highest velocities are nearest the outflow axis, and that the flow gently recollimates

Figure 5. Poloidal velocity fields of the 4 models, shown at the 4 different times in Fig. 2(a)

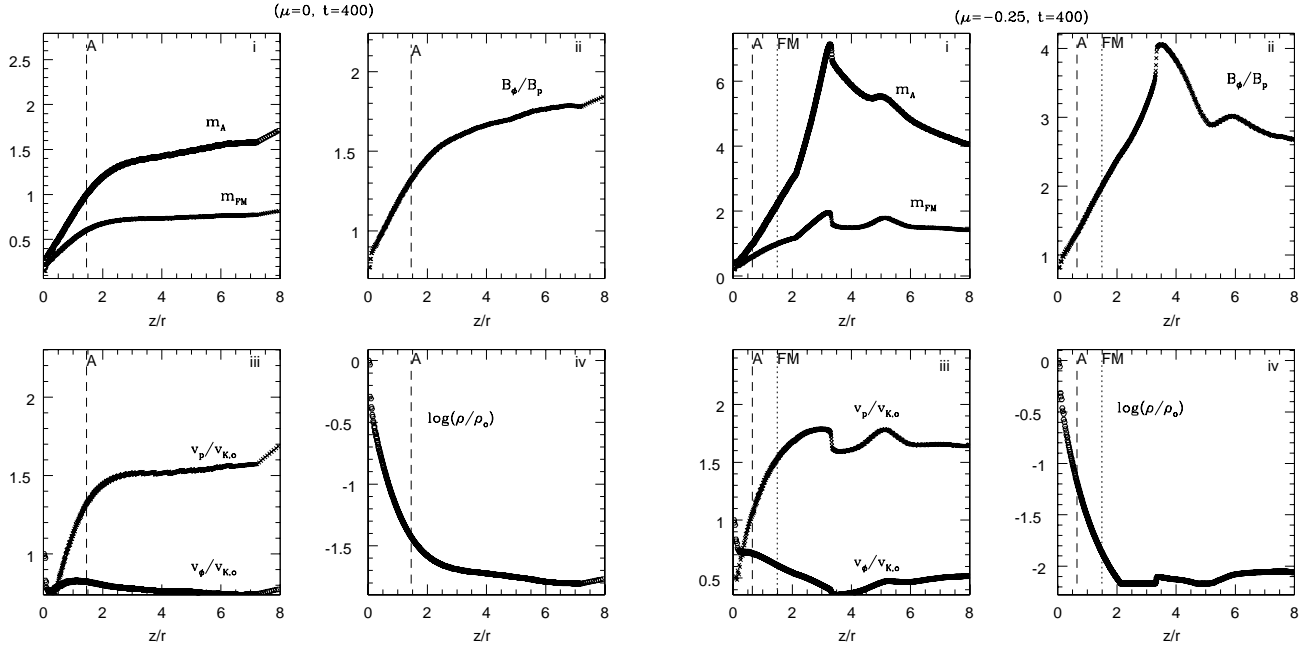


(c) PP92 case: The flow seems to be collimating in the early stages of the jet evolution, but as can be seen in the last panel, the flow assumes a conical geometry.



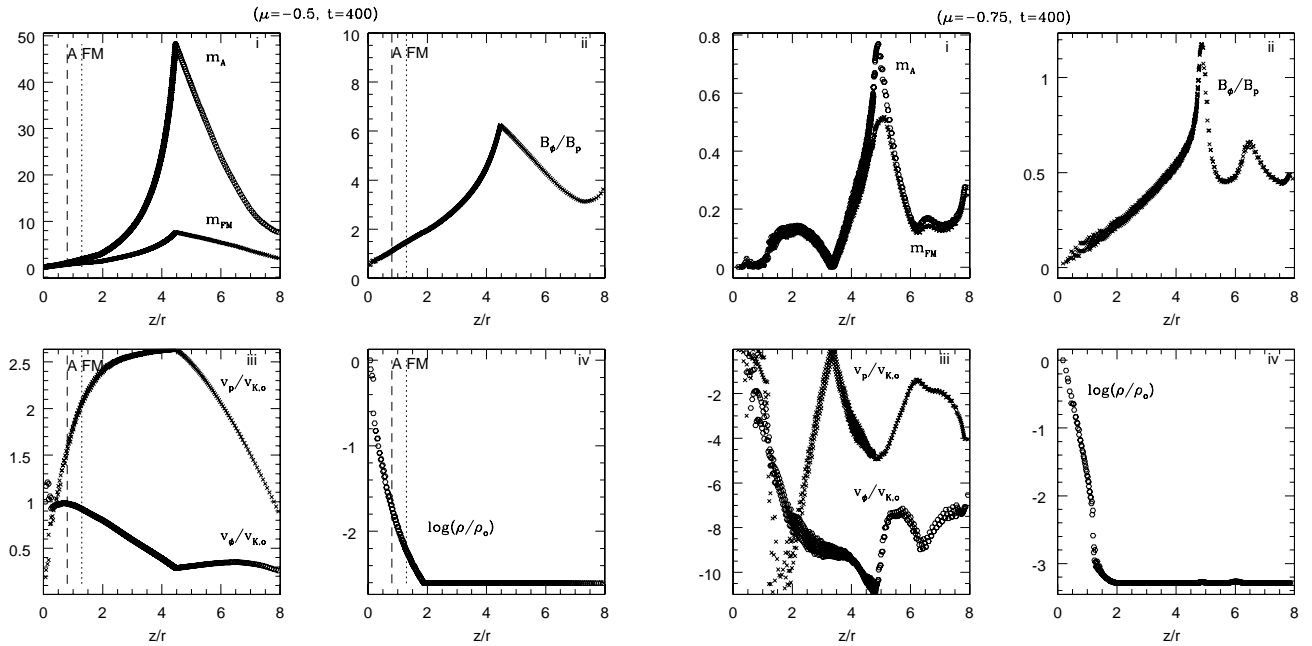
(d) 7Q case: The steepest configuration barely collimates at all and evolves differently from the other solutions. The wide-angle wind is even more extreme than the Pelletier-Pudritz solution

Figure 5. ...continued.



(a) Potential case

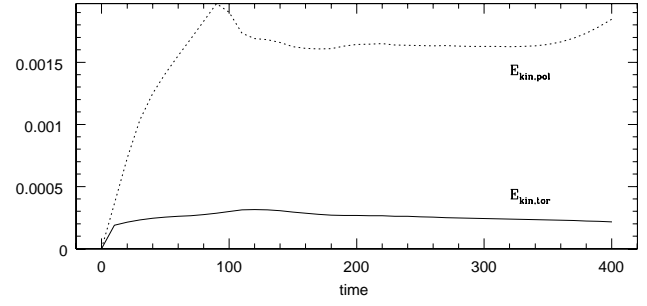
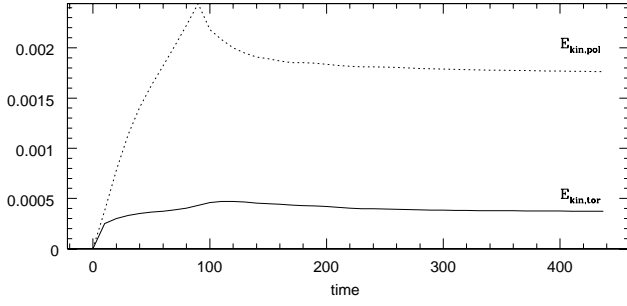
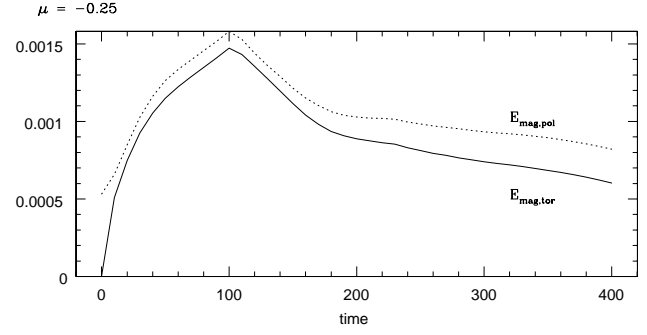
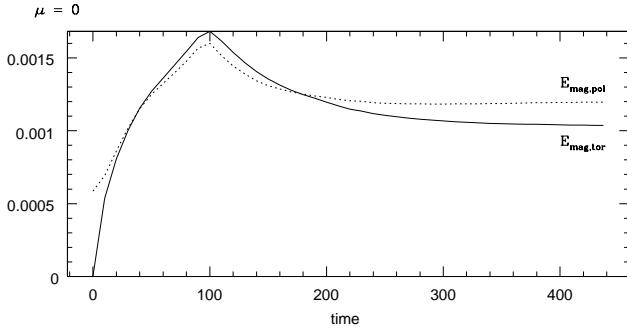
(b) BP82 case



(c) PP92 case

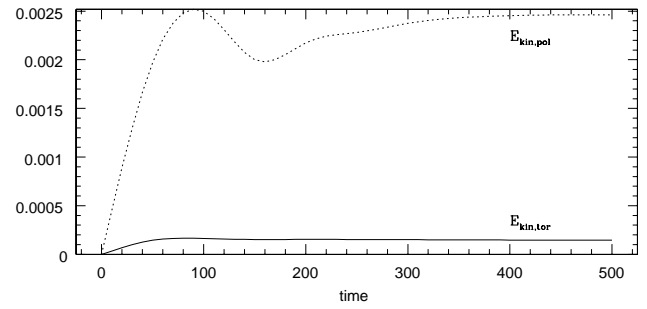
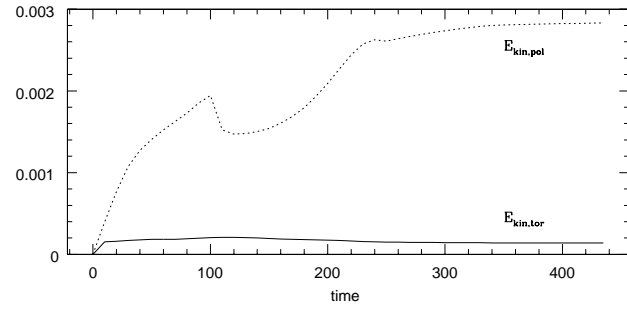
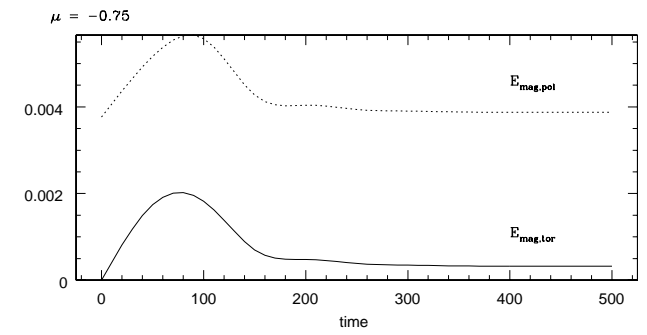
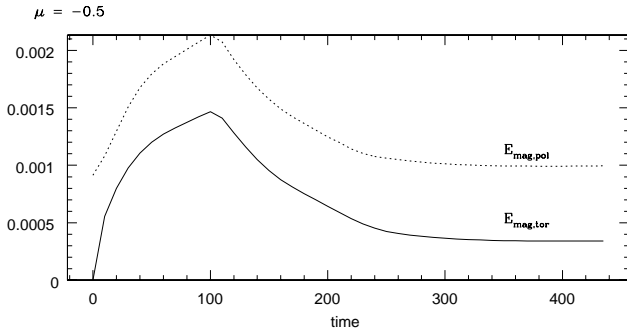
(d) 7Q case

Figure 6. Physical quantities along the fifth innermost fieldline, plotted against z/r . The position of the Alfvén and fast magnetosonic (marked by FM) critical points are shown.



(a) Potential case

(b) BP82 case



(c) PP92 case

(d) 7Q case

Figure 7. Quantification of the energies involved in the flow. In the upper/lower panel, the poloidal magnetic/kinetic energy is compared to the toroidal part. Note that the the poloidal magnetic energy in the last case is double that in the other cases.

Finally, the ratio of the toroidal to poloidal magnetic field along our illustrative field line clearly shows that the predominant magnetic field in jets beyond their FM surfaces is the toroidal field component. The stability of a jet that is dominated by a toroidal field is an important problem, and the 3D simulations needed to investigate the importance of kink modes are still rare. Our own 3D study of a jet in an initially uniform field (Ouyed, Clarke, & Pudritz 2003) shows that jets survive the threatening non-axisymmetric kink ($m = 1$) mode, and we plan to extend this work to these more general configurations.

5.3 Jet energetics

The bulk energetics of our 4 model outflows, as a function of time, are shown in 7(a)–7(d). In every case, we see that the jets end up being dominated by the poloidal kinetic energy of the jet, followed in magnitude by the energy in the poloidal magnetic field, and then the energy in the toroidal magnetic field. The lowest energy in all of the outflows is the energy in the overall rotation of the jet. Thus, we find that

$$E_{kin,pol} > E_{mag,pol} > E_{mag,tor} > E_{kin,tor} \quad (39)$$

These energies shown in this figure are given in units of the following physical quantities: the poloidal and toroidal kinetic energies are in units of $2\pi\rho_i v_{K,i}^2 r_i^3$, while the poloidal and toroidal magnetic energies are given in units of $(B_{p,i}^2/2)r_i^3$.

The ratios of the various energy terms are more interesting. In going through the 4 cases $\mu = 0$ to $\mu = -3/4$, these figures show that the ratio of the poloidal kinetic energy (bulk energy in outflow) to the bulk energy in the poloidal fields, takes the values:

$$\frac{E_{kin,pol}}{E_{mag,pol}} = 1.5, \quad 2.0, \quad 2.8, \quad 6.3. \quad (40)$$

This shows that the most efficient acceleration of the flows and the conversion of gravitational binding energy into bulk flow is from the less steeply raked mass loads - ie the flows that carry the most mass. We noted earlier that the PP92 solutions achieved the highest terminal Alfvén Mach numbers, which goes together with this result.

A comparison of the energy in the poloidal and toroidal field components is most revealing:

$$\frac{E_{mag,pol}}{E_{mag,tor}} = 1.2, \quad 1.3, \quad 2.5, \quad 8.0. \quad (41)$$

Clearly, the relative importance of the toroidal field becomes progressively less as one goes through this mass load sequence - exactly as our theoretical model predicts. The potential and BP82 solutions ($\mu = 0, -0.25$) both have toroidal magnetic energies comparable to their poloidal energies, whereas the other two solutions are dominated by the poloidal field component. While all four configurations have comparable toroidal magnetic energies (with the collimated solutions having more at later times), the energy of the poloidal magnetic field in the last case is almost three times larger than the others.

5.4 Jet rotation

The rotational velocity (left hand column) and toroidal magnetic field strength (right hand column) throughout the 4 outflows, are shown in Figure 8. As was found in the potential configurations of OPS97, the top panel in this figure shows a beautifully, well collimated outflow with the toroidal field components nearly constant along cylinders. This is also seen for the BP82 case although, not as strongly as the potential case. The wide-angle behaviour of the final two cases is apparent in both the toroidal velocity and field contours as well. The explanation for this wide-angle behaviour lies in the distribution and strength of the toroidal magnetic field (right panels), which is too weak to collimate the flow, as contrasted with the upper two cases, which clearly has a strong B_ϕ along the jet axis.

The radial profile of the rotation speed of material in the outflows are shown in Figure 9. The two columns show cuts at different distances z down the jet axis, the right hand column being within the Alfvén surface, while the left hand column is at high z . At high z , the outermost radial profiles of the outflow’s rotation speed for the first 3 models can be well fit by power laws;

$$v_\phi(r) \propto r^a \quad (42)$$

$$a = -0.76 \quad -0.66; \quad -0.46 \quad (43)$$

respectively, whereas the 7Q simulation is even flatter in profile but too variable to fit with a powerlaw at $t = 400$.

These rotational profiles are sufficiently different that it may be possible for future observations to place constraints on the precise nature of the mass load by mapping out the radial rotational profile, and using it to infer the underlying mass load.

6 DISCUSSION AND CONCLUSIONS

We have demonstrated that accretion disks play a major role in controlling the collimation of disk winds through the radial mass load profiles that they impose on these outflows. The conservation laws for stationary, axisymmetric outflows show that the toroidal field at any point in the jet is regulated by this mass load function. Given that the toroidal field is responsible for the collimating hoop stress in the jet, accretion disks can help determine the structure of jets and outflows far from their point of origin on the disk.

Our simulations divide into two classes - those that achieve collimation towards a cylinder, and those that have a wide-angle structure. We showed that these correspond quite well to predictions made by HN89 about jet collimation, namely, that if the current $I(r)$ goes to zero in the limit of large jet radius, that such field lines would have a parabolic structure, whereas currents that remain finite or diverge result in jets that collimate cylindrically.

We argue that the differences between wide-angle and highly collimated jets and outflows inferred in the observational literature, are two aspects of the same underlying mechanism. Hydromagnetic disk winds can achieve both types of configuration depending on the mass loading that takes place in the underlying accretion disk. Specifically,

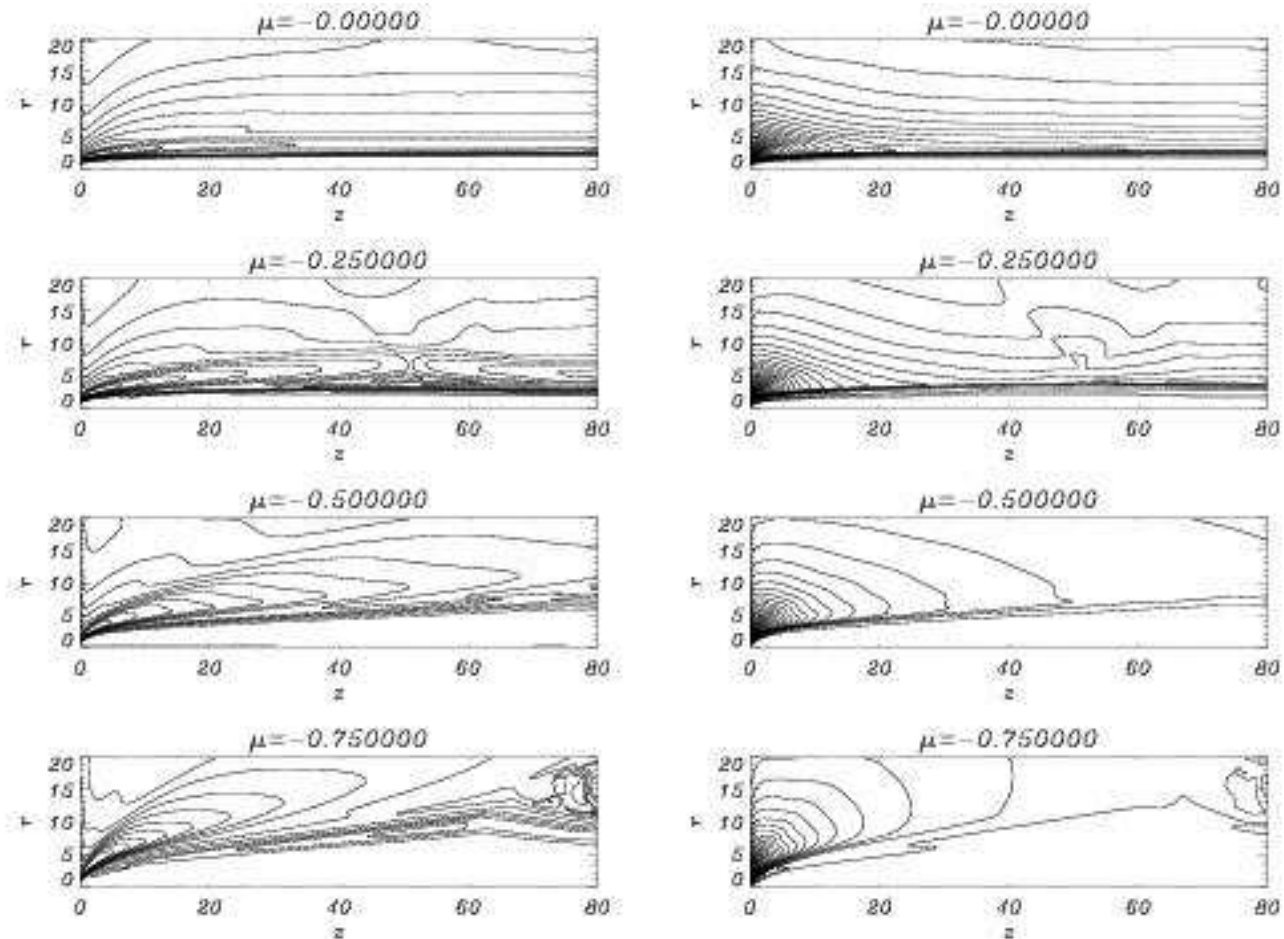


Figure 8. Contours of the toroidal velocity (left panels) and toroidal magnetic field (right panels) at $t = 400$ for the four cases. This figure can be compared to 5(a)-5(d). Note that the magnetic field in the last two panels is too weak to collimate the flow.

we find that the potential and Blandford-Payne magnetic field distributions $B_p(r_o) \propto r_o^{-1}, r_o^{-5/4}$ respectively, result in mass loading profiles that produce cylindrically collimated jets. The Pelletier-Pudritz configuration on the other hand, $B_p(r_o) \propto r_o^{-3/2}$ results in a finite current and is the boundary between cylindrically and parabolically collimated outflows. It may be that nature produces magnetic configurations in accretion disks that arise through an optimization process (eg. minimum magnetic energy configuration) of some kind. We speculate that it may be that small fluctuations in jet mass loading, about an energetically preferred PP92 profile, would result in jets that are either cylindrically, or parabolically (ie wide-angle) collimated. This could explain the variety of jet collimations that are suggested by the observations.

Our results allow one to understand why simulation of X-winds by Shu et al. (2000), or split monopoles by Romanova et al (1997) result in wide-angle flows whose field lines do not collimate towards the outflow axis. This is a consequence of having steep magnetic field gradients, and hence shallow mass loading profiles which, as we have seen, result in weak toroidal fields in the jet. These are unable to collimate the nearly radial field lines. As Shu et al. (2000) note, this does not prevent the densest material in the out-

flow from concentrating in flow that is parallel to the outflow axis. We see this in all of our simulations.

The radial profiles of various outflow quantities such as the poloidal outflow speed v_{pol} are tabulated in this paper. Our outflows all show the "onion-layer" velocity structure that are revealed by the observations of protostellar jets, namely, that the highest velocity gas is in the interior of the jet while the lower velocity material are found at increasingly larger outflow radii. Of particular interest is the behaviour of jet rotation $v_\phi(r) \propto r^a$ as one goes radially through the jet. We find that this distribution depends on the underlying mass load (and hence magnetic configuration in these simulations). Specifically, $a = -0.76, -0.66, -0.46$ as one goes from the potential configuration, to the Blandford-Payne distribution, and on to the Pelletier-Pudritz distribution of disk fields $\mu = 0, -1/4, -1/2$ respectively.

In conclusion, this paper shows that accretion disks can exert a long-range control of jet properties such as their collimation and spin, as a consequence of their mass loading. What remains to be clarified is exactly how the accretion disk actually does this. It may be that the accretion disk corona plays an important role in this process. Dynamical 3D global simulations of the disk and its outflow, as now

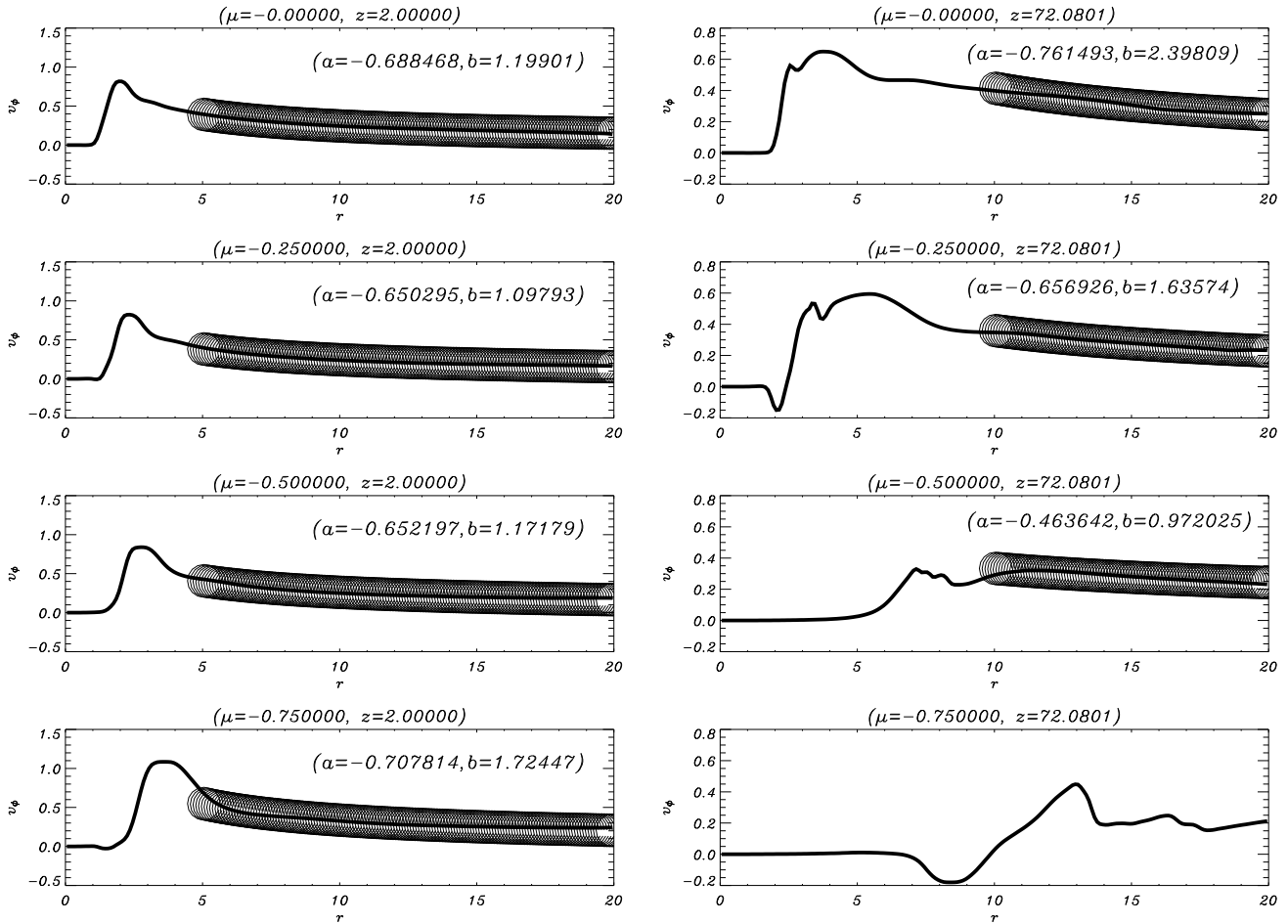


Figure 9. Radial profiles of the toroidal velocity within the Alfvén surface (left panels) and at high z (right panels) for each solution at $t = 400$. The sub-Alfvénic flow can easily be fit by a power law. At high z , only the outermost radii can be well fit, while the steepest case still exhibits complex behaviour.

being carried out by an increasing number of authors, may offer the best way of exploring the physics of this problem.

ACKNOWLEDGEMENTS

We thank T. Ray and G. Pelletier for stimulating conversations about these topics, and the organizers and lecturers of the Les Houches School on accretion disks and jets (held in summer 2002) for the stimulating intellectual atmosphere and incomparable mountain vistas that did much to stimulate the work in this paper. REP and RO are supported by grants from NSERC of Canada. CSR Rogers was supported by McMaster University and wishes to thank his parents for their encouragement to pursue his goals and ask questions, and *Google*TM for answering the questions no one else could.

REFERENCES

- Anderson W.L., 1979, *Geophysics*, 44, No.7, 1287.
- Anderson, J. M., Li, Z.-Y., Krasnopolsky, R., & Blandford, R. 2003, 590, L107
- Anderson, J. M., Li, Z.-Y., Krasnopolsky, R., & Blandford, R. 2005 [astro-ph/0410704]
- Bacciotti F., Ray, T.P., Mundt, R., Eilöffel, J., Solf, J., & Camenzind, M. (2000), 537, L 49.
- Bacciotti, F., Ray, T.P., Mundt, R., Eilöffel, J., & Solf, J. (2002), *ApSS*, 297, 3.
- Bacciotti, F., Testi, L., Marconi, A., Garcia, P. J. V., Ray, T.P., Mundt, R., Eilöffel, J., & Dougados, C. 2003, *ApSS*, 286, 157
- Bacciotti, F., Ray, T.P., Eilöffel, J., Woitas, J., Solf, J., Mundt, R., & Davis, C. J. 2003, *ApSS*, 287, 3
- Begelman, M. C., Blandford, R. D., & Rees, M. (1984), *Rev. Mod. Phys.*, 56, 255.
- Blandford, R. D., & Payne, D. G. 1982, *MNRAS*, 199, 883 (BP82)
- Cabrit, S., Raga, A. C., & Gueth, F. 1997, in *Herbig-Haro Flows and the Birth of Low Mass Stars*, B. Reipurth and C. Bertout, Dordrecht: Kluwer, 163
- Calvet, N., Hartmann, L., & Kenyon, S. J. 1993, *ApJ*, 402, 623
- Calvet, N. 2003, in *NATO ASI Les Houches Lectures on "Accretion disks, jets and high energy phenomena in astrophysics"*; V. Beskin, G. Henri, F. Menard, G. Pelletier, & J. Dalibard (eds.) (Springer-Verlag: Berlin), p. 521.

Casse, F., & Ferreira, J. 2000, *A&A*, 353, 1115.
 Coffey, D., Bacciotti, F., Woitas, J., Ray, T.P., & Eisloffel 2004, *ApJ*, 604, 758.
 Dougados, C., Cabrit, S., Lavalley, C., & Ménard, F. 2000, *A&A*, 357, L61.
 Fendt, C., & Elstner, D. 1999, *A&A*, 349, L61.
 Fendt, C. & Čemeljić, M. 2002, *A&A*, 395, 104.
 Goodson, A. P., Winglee, R. M., & Böhm, K.-H. 1997, *ApJ*, 489, 199.
 Hartmann, L., & Calvet, N. 1995, *AJ*, 109, 1846
 Hayashi, M.R., Shibata, K., & Matsumoto, R. 1996, *ApJL*, 468, L37.
 Heyvaerts, J., & Norman, C. A. 1989, *ApJ*, 347, 1055.
 Heyvaerts, J. 2003, in NATO ASI Les Houches Lectures on "Accretion disks, jets and high energy phenomena in astrophysics"; V. Beskin, G. Henri, F. Menard, G. Pelletier, & J. Dalibard (eds.) (Springer-Verlag: Berlin), p. 3.
 Keppens, R., & Goedbloed, J. P. 2000, *ApJ*, 530, 1036
 Königl, A. 1989, *ApJ*, 342, 208.
 Königl, A., & Pudritz, R.E. 2000, in Protostars & Planets IV, V. Mannings, A.P. Boss, & S.S. Russell (eds.) (Tucson: Univ. Arizona Press), p. 759.
 Krasnopolsky, R., Li, Z-Y, & Blandford, R.D. 1999, *ApJ*, 526, 631.
 Kudoh, T., Matsumoto, R., & Shibata, K. 2002, *PASJ*, 54, 121.
 Kwan, J., & Tademaru, E. 1988, *ApJ*, 332, L41.
 Lee, C-F, Mundy, L.G., Reipurth, B., Ostriker, E.C., & Stone, J.M. 2000, *ApJ*, 542, 925.
 Li, Z.-Y. 1995, *ApJ*, 444, 848.
 Matt, S., & Balick, B. 2004, *ApJ*, 615, 921.
 Matt, S., & Pudritz, R.E. 2004, *ApJL*, 607, L43.
 Meier, D.L., Eddington, S., Godon, P., Payne, D.G., & Lind, K.R. 1997, *Nature*, 388, 350.
 Mestel, L. 1968, *MNRAS*, 138, 359.
 Mirabel, I.F., & Rodriguez, L.F. 1998, *Nature*, 392, 673.
 Ouyed, R., & Pudritz, R. E. 1997a, *ApJ*, 482, 712 (OP97a).
 Ouyed, R., & Pudritz, R. E. 1997b, *ApJ*, 484, 794 (OP97b).
 Ouyed, R., Pudritz, R. E., & Stone, J. M. 1997, *Nature*, 385, 409 (OPS97).
 Ouyed, R., & Pudritz, R. E. 1999, *MNRAS*, 309, 233 (OP99).
 Ouyed, R., Clarke, D. A., & Pudritz, R. E., 2003, *ApJ*, 582, 292
 Ostriker, E. 1998, *ApJ*, 486, 291.
 Piessens, R., 1982 "Automatic Computation of Bessel Function Integrals", *Computer Physics Comm.* 25, p 289-295.
 Pelletier, G., & Pudritz, R. E. 1992, *ApJ*, 394, 117 (PP92).
 Pudritz, R.E 2003, in NATO ASI Les Houches Lectures on "Accretion disks, jets and high energy phenomena in astrophysics"; V. Beskin, G. Henri, F. Menard, G. Pelletier, & J. Dalibard (eds.) (Springer-Verlag: Berlin), p. 187.
 Pudritz, R.E., & Banerjee, R. 2005, in IAU Symposium 227 on "Massive Star Birth: A Crossroads of Astrophysics"; R.Cesaroni, M. Felli, E. Churchwell, & C.M. Walmsley, eds.
 Reipurth, B., & Bally, J. 2001, *ARA&A*, 39, 403.
 Richer, J.S., Shepherd, D.S., Cabrit, S., Bachiller, R., & Churchwell, E. 2000, in Protostars & Planets IV, V. Mannings, A.P. Boss, & S.S. Russell (eds.) (Tucson: Univ. Arizona Press), p. 867.

Romanova, M. M., Ustyugova, G. V., Koldoba, A.V., Chechetkin, V.M., & Lovelace, R. V. 1997, *ApJ*, 482, 708.
 Sakurai, T. 1985, *A&A*, 152, 121.
 Shepherd, D. 2005, in IAU Symposium 227 on "Massive Star Birth: A Crossroads of Astrophysics"; R.Cesaroni, M. Felli, E. Churchwell, & C.M. Walmsley, eds.
 Shu, F.H., Najita, J., Shang, H., & Li, Z.-Y. 2000, in Protostars & Planets IV, V. Mannings, A.P. Boss, & S.S. Russell (eds.) (Tucson: Univ. Arizona Press), p. 789.
 Spruit, H.C. 1996, in NATO ASI, Evolutionary processes in binary stars, R.A.M.J. Wijers, M.B. Davies, & C.A. Tout (eds.) (Dordrecht: Kluwer), p. 249.
 Stone, J.M., & Norman, M.L. 1992, *ApJS*, 80, 753
 Stone, J.M., & Norman, M.L. 1994, *ApJ*, 433, 746.
 Tomisaka, K. 1998, *ApJ*, 502, L163.
 Trussoni, E., Tsinganos, K., & Sauty, C. 1997, *A&A*, 325, 1099
 Tsinganos, K., & Trussoni, E. 1990, *A&A*, 231, 270.
 Ustyugova, G.V. et al., 1998, *ApJ*, 500, 703.
 von Rekowski, B. & Brandenburg, A. 2004, *A&A*, 420, 17
 Weber, E. J., & Davis, L. 1967, *ApJ*, 148, 217.
 Zhang, Q. 2005, in IAU Symposium 227 on "Massive Star Birth: A Crossroads of Astrophysics"; R.Cesaroni, M. Felli, E. Churchwell, & C.M. Walmsley, eds.

APPENDIX A: COMPUTING THE INITIAL CONFIGURATION OF THE MAGNETIC FIELDS

First, we assume axisymmetry, and thus all $\frac{\partial}{\partial \phi}$ terms are ignored. Second, we are considering only poloidal components; all toroidal magnetic field arises from the centrifugal motion of the disk. If we take the magnetic field as

$$\mathbf{B} = \nabla \times \mathbf{A} \quad (\text{A1})$$

then

$$B_r = -\frac{\partial A_\phi}{\partial z}; \quad (\text{A2})$$

$$B_\phi = 0; \quad (\text{A3})$$

and

$$B_z = -\frac{1}{r} \frac{\partial r A_\phi}{\partial r} \quad (\text{A4})$$

Thus it remains to find some function A_ϕ which satisfies our boundary and initial conditions. We considered only solutions that were current-free, thus keeping the Lorentz force $\mathbf{F} = \mathbf{J} \times \mathbf{B}$ on the object also equal to zero. Since $\mathbf{J} = \nabla \times \mathbf{B}$, this means the current-free condition can be written

$$\frac{\partial B_r}{\partial z} - \frac{\partial B_z}{\partial r} = 0 \quad (\text{A5})$$

which gives us a separable equation for A_ϕ :

$$\frac{\partial^2 A_\phi}{\partial r^2} + \frac{1}{r} \frac{\partial A_\phi}{\partial r} - \frac{A_\phi}{r^2} = -\frac{\partial^2 A_\phi}{\partial z^2} = -k^2 \quad (\text{A6})$$

with (non-divergent) basis functions $A_{\phi,k}$

$$A_{\phi,k} = J_1(kr) \exp(-k|z|) \quad (\text{A7})$$

yielding a general class of solutions

$$A_\phi(r, z) = \int_0^\infty S(k) J_1(kr) \exp(-k|z|) dk \quad (\text{A8})$$

It now remains to find the amplitude $S(k)$, from some boundary condition. We exploit this freedom and let B_z in the disk have a radial dependence given by:

$$B_z(r, z = 0) = br^{\mu-1} \quad (\text{A9})$$

where b is a normalizing constant.

Using Eqn A.4 and A.8 and exploiting the properties of Bessel functions, we have the following form for B_z :

$$B_z(r, z = 0) = \int_0^\infty S(k) J_0(kr) k dk \quad (\text{A10})$$

The inverse Hankel Transform gives us an equation for $S(k)$

$$\begin{aligned} S(k) &= \int_0^\infty B_z(r, z = 0) J_0(kr) r dr \\ &= b \int_0^\infty r^\mu J_0(kr) dr \end{aligned} \quad (\text{A11})$$

which has the solution

$$S(k) = \frac{b}{k^{\mu+1}} f(\mu) \quad (\text{A12})$$

where

$$f(\mu) = 2^\mu \frac{\Gamma(1/2 + \mu/2)}{\Gamma(1/2 - \mu/2)} \quad (\text{A13})$$

(Note that this analytic transform was useful for testing our numerical integrator, as explained in the next section.)

Thus, equation A.8 becomes

$$A_\phi(r, z) = bf(\mu) \int_0^\infty \frac{1}{k^{\mu+1}} J_1(kr) \exp(-k|z|) dk \quad (\text{A14})$$

This Hankel transform has only two analytical solutions, when $\mu = +1$, which has vertical field lines ($B_z = b$, where b is a constant), and when $\mu = 0$, which is the potential solution discussed in OPI.

We employed a numeric integrator to evaluate three additional configurations, approaching the lower limit of $\mu = -1$; $\mu = -1/4$, which corresponds to the self-similar solutions of BP82, $\mu = -1/2$, the solution suggested by PP92, and $\mu = -3/4$.

APPENDIX B: HANKEL TRANSFORM ALGORITHM

Since there are a bevy of Hankel transform algorithms available in the public domain, it was unnecessary to devise our own. In our search for a numeric integration program capable of performing Hankel transforms, we tested several applications. The two most tested programs were designed by Anderson (1979); Piessens (1982). The most important criteria for our choice were speed and accuracy. The initial conditions for our 500x200 grid were set point by point, so it was important that the transforms be done quickly and efficiently.

Piessens' program 'hankel' is a double-precision code using Fast Fourier Transforms (which are done by gaussian quadrature methods) to evaluate each transform. It ran somewhat slowly, and the solutions it gave did not behave

well near the analytic limits ($\mu = -1, +1$) of the functions we were evaluating. It was capable of integrating Bessel functions of any order, but since our transforms were only of order 0 and 1, this feature was unnecessary. Anderson's program 'ZHANKS' (Anderson 1979) is a single precision code that uses adaptive filter weights. The filters are designed by using Hankel Transforms with known analytic solutions:

$$\int_0^\infty \lambda \exp(-a\lambda^2) J_0(b\lambda) d\lambda = [\exp(-b^2/4a)]/(2a) \quad (\text{B1})$$

and

$$\int_0^\infty \lambda^2 \exp(-a\lambda^2) J_1(b\lambda) d\lambda = b[\exp(-b^2/4a)]/(2a)^2 \quad (\text{B2})$$

where $a > 0, b > 0$.

Its algorithm uses the fact that algebraically related kernel functions (the function being transformed by convolution with the Bessel function) transform the same way. Thus, the computed kernel function is saved on its first call, and subsequent calculations use the results of previous calculations to evaluate the transforms, making computation much faster. The solutions computed by the ZHANKS algorithm are also behaved better at the analytic limits, matching closely with the solutions we tested using MATLAB.

In addition to comparisons with known analytic solutions, the results of the algorithms were tested in a hydrostatic run of our simulation in which the disk did not rotate. Since the corona was in pressure balance with the central star and the surrounding disk, only magnetic forces would disturb the gas. As the initial conditions should be completely current-free, no Lorentz forces should be developed, and the gas should remain motionless. This was in fact the case, except for slight motions arising from a combination of the accuracy of the algorithms and the discrete nature of the grid. Our hydrostatic simulations were run out beyond 400 timesteps for each magnetic configuration. The motions were slightly increased for the more radially dependent magnetic profiles ($\mu = -1/2$ and $\mu = -3/4$), but in all cases their movement was such that the hydrostatic balance was disturbed to no more than $5r_i$ after $400t_i$

